Available online at www.sciencedirect.com

ScienceDirect

Underground Space 25 (2025) 387–409

www.keaipublishing.com/undsp

Research Paper

Influence of water content on the failure modes and macro-micromechanical properties of sulfate rocks: Insights from experimental and DEM simulations

Li Yu [a,b], Youlin Qin [a,b,*], Hualao Wang [c], Mingnian Wang [a,b], Zhaohui Chen [a,b], Mingyang Yu [a,b], Hong Jin [a,b]

[a] School of Civil Engineering, Southwest Jiaotong University, Chengdu 610036, China
[b] State Key Laboratory of Intelligent Geotechnics and Tunnelling, Chengdu 610036, China
[c] Bridge and Tunnel Research Center, Research Institute of Highway of Ministry of Transport, Beijing 100088, China

Received 27 February 2025; received in revised form 8 May 2025; accepted 4 June 2025
Available online 15 October 2025

Abstract

The initial water content significantly affects rock mechanics, especially with swelling minerals. However, the effects of initial water content on the mechanical properties and failure mode of sulfate rocks remain unclear. This study explores these effects by conducting unconfined compressive strength (UCS) experiments and discrete element method simulations on sulfate rocks. The results indicate that as the initial water content increased from 0 to 9%, the Young's modulus and Poisson's ratio of sulfate rock exponentially decreased by 48.9% and 290%, respectively. Additionally, the crack initiation stress (σ_{ci}), crack damage stress (σ_{cd}), and UCS decreased by 62.4%, 51.5%, and 53.3%, respectively. The stress responses to initial water content follow linear functions. Notable decreases were also observed in the normal and shear stiffness parameters (k_n and k_s) of contact, diminishing by 46.53% and 46.54%, respectively; peak cohesion decreased by 69.70%; peak friction angle by 17.39%; peak tensile strength by 124%. Rising initial water content leads to increased damage and softening of sulfate rock, causing decreased mechanical properties. It can be observed that as the initial water content increases, the proportion of micro-tensile fractures in the total number of fractures increases, and the dominant failure mode of sulfate rock gradually transitions from shear to tensile failure.

Keywords: Sulfate rock; Anhydrite; Initial water content; Failure model; 3DEC-GBM

1 Introduction

Sulfate rock consists of both a clay matrix and finely dispersed anhydrite minerals (Schweizer et al., 2018). The clay and anhydrite minerals have the ability to absorb water. The volume increase due to the absorption of water by anhydrite and clay minerals is called rock swelling. Water access induces swelling of expansion minerals, simultaneously leading to damage to the microstructure inside the rock. This swelling phenomenon is accompanied by changes in the mechanical properties of the rock. All over the world, there have been large engineering disasters in tunnels crossing sulfate rock formations, such as tunnel floor heave, lining destruction, and reduction of the effective cross-sectional area of tunnels, as shown in Fig. 1 (Alonso et al., 2013; Liu et al., 2011; Serafeimidis et al., 2013; Xu et al., 2021; Zhang et al., 2017). These issues are partly attributed to the influence of swelling and partly to changes in rock mechanical properties caused by swelling after absorbing water. Therefore, for engineering design, the swelling characteristics and mechanical properties of sulfate rock are of utmost concern to technicians. Changes in mechanical properties can also alter the failure

* Corresponding author at: School of Civil Engineering, Southwest Jiaotong University, Chengdu 610036, China.
E-mail address: ylqin@my.swjtu.edu.cn (Y. Qin).
Peer review under the responsibility of Tongji University

https://doi.org/10.1016/j.undsp.2025.06.005

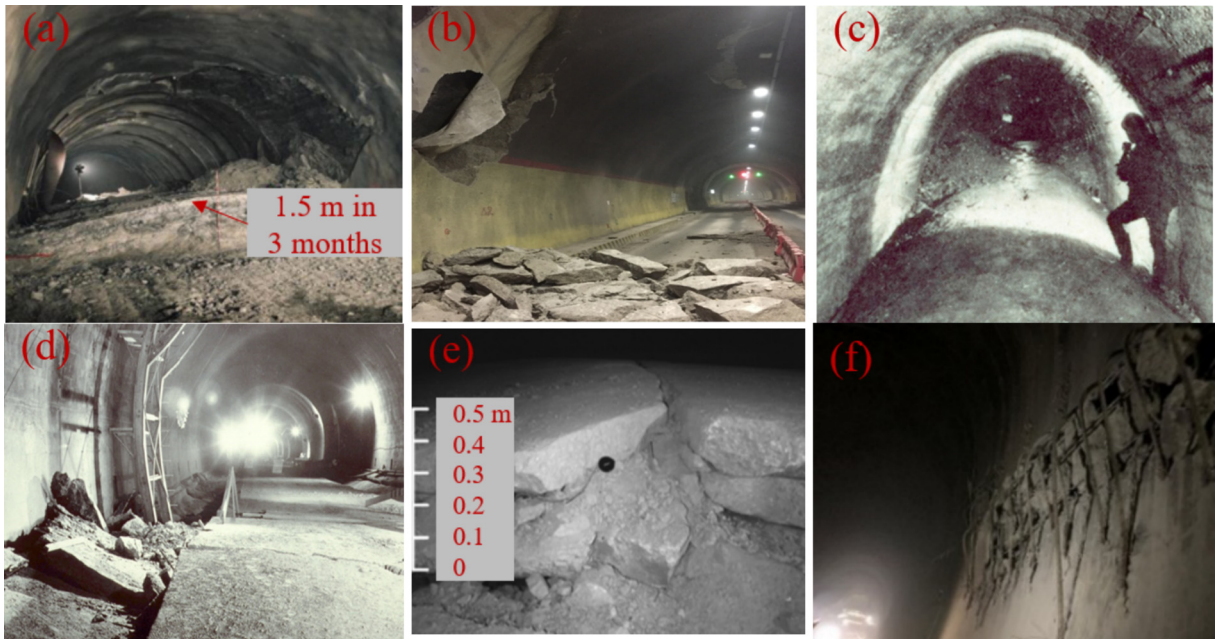

Fig. 1. Serious diseases of tunnel due to sulfate rock. (a) Invert heave in Chienberg tunnel, (b) lining structure failure of the Dugongling tunnel, (c) heave of invert in Wagenburg tunnel, (d) heave of floor in the Belchen tunnel, (e) heave and failure of the tunnel flat-slab in Lilla tunnel, and (f) lining structure failure of the South Lvliang tunnel.

mode of rocks (Yan et al., 2023). Water has a significant effect on these properties of rock (Hu et al., 2014; Liu et al., 2021; Maximiliano & Triantafyllidis, 2016), especially swelling rocks that are extremely sensitive to water. In contrast to swelling properties, the effects of initial water content on the mechanical properties and failure behavior of sulfate rock remain ambiguous. It is suggested that investigating the effect of water on this relationship is of significant importance in sulfate rock and represents an attractive topic for engineering construction.

Swelling rocks are categorized as physical (e.g., clay rocks) or chemical (e.g., sulfate rocks). Clay rocks, typically soft and water-sensitive, often soften or disintegrate upon wetting (Cherblanc et al., 2016; Zhang & Wu, 2020; Zhong et al., 2019). Consequently, their mechanical properties—particularly elastic modulus and failure strength—are highly sensitive to initial water content (Bornert et al., 2010; Hu et al., 2014; Zhang & Rothfuchs, 2004). Numerous studies have experimentally examined how water content affects parameters such as elastic modulus, tensile strength, and compressive strength, and have developed corresponding predictive models (Hu et al., 2014; Liu et al., 2021; Maximiliano & Triantafyllidis, 2016; Vásárhelyi, 2005; Vásárhelyi & Ván, 2006). Furthermore, the mechanisms by which water weakens these properties have also been explored (Li et al., 2022; Liu et al., 2021; Maximiliano & Triantafyllidis, 2016; Yang & Du, 2016; Zhang et al., 2020).

Unlike the single physical swelling of clay minerals in clay rock, the swelling of sulfate rock results from two overlapping processes upon water absorption: (i) the physical swelling of clay due to osmotic water uptake and hydration, and (ii) the chemical transformation of anhydrite ($CaSO_4$) into gypsum ($CaSO_4 \cdot 2H_2O$) when in contact with water ($CaSO_4 + 2H_2O = CaSO_4 \cdot 2H_2O$) (Alonso et al., 2013; Butscher et al., 2018, 2016; Schweizer et al., 2018; Serafeimidis & Anagnostou, 2013, 2015). The chemical reaction is the dominant mechanism and generates swelling pressures several times greater than those in clay rocks (Butscher et al., 2018, 2016; Pimentel & Anagnostou, 2013; Steiner, 1993). Swelling pressures reaching several MPa have led to severe engineering problems (Alonso et al., 2013; Alonso & Ramon, 2013; Butscher et al., 2011; Liu et al., 2011; Serafeimidis & Anagnostou, 2013; Xu et al., 2021). Consequently, research on sulfate rock has primarily focused on its swelling pressure and associated constitutive relationships derived from experiments (Alonso et al., 2013; Pimentel & Anagnostou, 2013; Pimentel, 2015; Serafeimidis & Anagnostou, 2014, 2015), often neglecting the effect of water on its mechanical properties. Although some studies have measured the compressive strength, elastic modulus, peak strain, and internal friction angle of pure anhydrite rock (Gao et al., 2011; Su et al., 2019; Zhu et al., 2013), they seldom consider the influence of initial water content. Moreover, pure anhydrite rock lacks clay minerals, which—despite their lower swelling potential compared to anhydrite—still play a significant role in the overall swelling behavior (Madsen & Nuesch, 1991). This distinction underscores the fundamental differences between the two rock types and suggests that mechanical properties derived from pure anhydrite are not representative of sulfate rock. In summary, experimental studies focusing on the effect of initial water content on the mechanical properties of sulfate rock are scarce. Even

under otherwise identical conditions, variations in initial water content lead to differences in water absorption capacity and initial mechanical properties. As such, neglecting the impact of initial water content on the macro- and meso-mechanical properties and failure behavior of sulfate rock is insufficient for addressing the design and construction challenges in sulfate-rich tunnel environments.

In recent decades, numerical simulation techniques, grounded in laboratory experimental research, have been extensively used for the quantitative analysis of rock mechanical properties. These methods are generally classified into two main categories: continuum-based approaches, such as the finite element method (FEM) and finite difference method (FDM), and discontinuum-based approaches, including the finite-discrete element method (FDEM), discrete element method (DEM), and discontinuous deformation analysis (DDA) (Li et al., 2019). For example, Mardalizad et al. (2018) applied FEM-based simulations to examine the unconfined compressive strength (UCS) and failure processes of rocks, while Inga et al. (2023) combined DEM with Brazilian splitting tensile tests to assess rock mechanical behavior. Numerous studies (Alejano et al., 2017; Huang et al., 2023; Sinha et al., 2020) have utilized DEM to systematically investigate rock failure under uniaxial compression, providing insight into underlying failure mechanisms. Although DEM is generally more computationally intensive than continuum methods, it offers distinct advantages in modeling rock fracture and crack evolution. Specifically, DEM can capture both macroscopic mechanical responses and microscopic crack initiation and propagation (Li et al., 2020; Turichshev & Hadjigeorgiou, 2017; Zhang et al., 2025). Therefore, this study adopts the DEM approach to explore the failure modes and macro-micromechanical behavior of sulfate rocks.

This study examines the effect of initial water content on the macro- and meso-mechanical properties and failure modes of sulfate rock through laboratory and 3D grain-based model (GBM). UCS tests were performed on specimens with 0, 3%, 6%, and 9% water content. A novel 3D GBM was developed in 3DEC to realistically simulate fracturing, and its accuracy was validated against experimental data. Finally, the combined results of laboratory and numerical experiments comprehensively revealed the effects of initial water content on the mechanical properties, microcracking process, characteristic stress, and failure modes of sulfate rock.

2 Test materials and methods

2.1 Materials

The study area is located in Linfen City, Shanxi Province, China, approximately at 36°05′N and 111°30′E. An intact block of sulfate rock was selected from a sulfate rock stratum within a 23.4-km-long tunnel, at a depth of over 500 m, as shown in Fig. 2(a).

According to the X-ray diffraction (XRD) analyses, a portion of the results is presented in Fig. 3. The rock consists of gypsum, anhydrite, muscovite, kaolinite, quartz, smectite, and celestite. Gypsum constitutes an average mass fraction of 55.9% in the rock block, anhydrite 24.3%, muscovite 8.6%, quartz 4.0%, celestite 0.8%, and the clay minerals, including kaolinite and smectite, total 6.4%. All the specimens in this experiment originated from the same block of sulfate rock, as shown in Fig. 2(b).

2.2 Samples preparation

The block was sent back to the laboratory for slow cutting on a high-precision cutting machine to obtain cylindrical samples (with a diameter of 50 mm and a height of 100 mm). To avoid the influence of water on the mechanical properties of the sulfate rock samples, both cutting and section polishing were performed using the air flushing method.

After cutting and polishing, the sample preparation process is shown in Fig. 4. Initially, the rock samples were weighed, measured, and photographed, as shown in Fig. 4(a)–(c). Subsequently, the natural samples were dried in an oven at 220 °C for 24 h to convert gypsum into anhydrite (Su et al., 2019; Xu et al., 2019), as shown in Fig. 4(d). The dried samples were then reweighed to determine their dry mass (Fig. 4(e)). To obtain samples with varying initial water content, the specimens were conditioned in a controlled environment with a constant temperature of 21 °C and relative humidity (RH) of 90% (Pimentel & Anagnostou, 2013), under atmospheric pressure measured at 101.2 kPa, as shown in Fig. 4(f). During wetting, the samples were weighed every two hours (Fig. 4(g)) until the target water content was achieved, calculated using Eq. (1). The preparation was considered complete when the specimen mass reached $m_0(1 + w_t)$. Finally, the test samples were prepared with initial water content levels of 0, 3%, 6%, and 9%. It is crucial to note that once prepared, the water-bearing samples were immediately wrapped in plastic and stored in a dry, sealed environment to prevent water loss.

$$w_t = (m_1 - m_0)/m_0 \times 100\%, \tag{1}$$

where w_t is the initial water content of the sample, m_1 is the wet mass of the sample, and m_0 is the dry mass of the sample.

Post-experimental observations of the specimens reveal that the gypsum texture of the studied rock is predominantly vein-like with a fibrous, as shown in Fig. 5.

2.3 Testing procedures

After completion of the sample preparation, unconfined compressive strength (UCS) tests were undertaken on different water-bearing samples, with initial water content of 0, 3%, 6%, and 9%, as shown in Table 1.

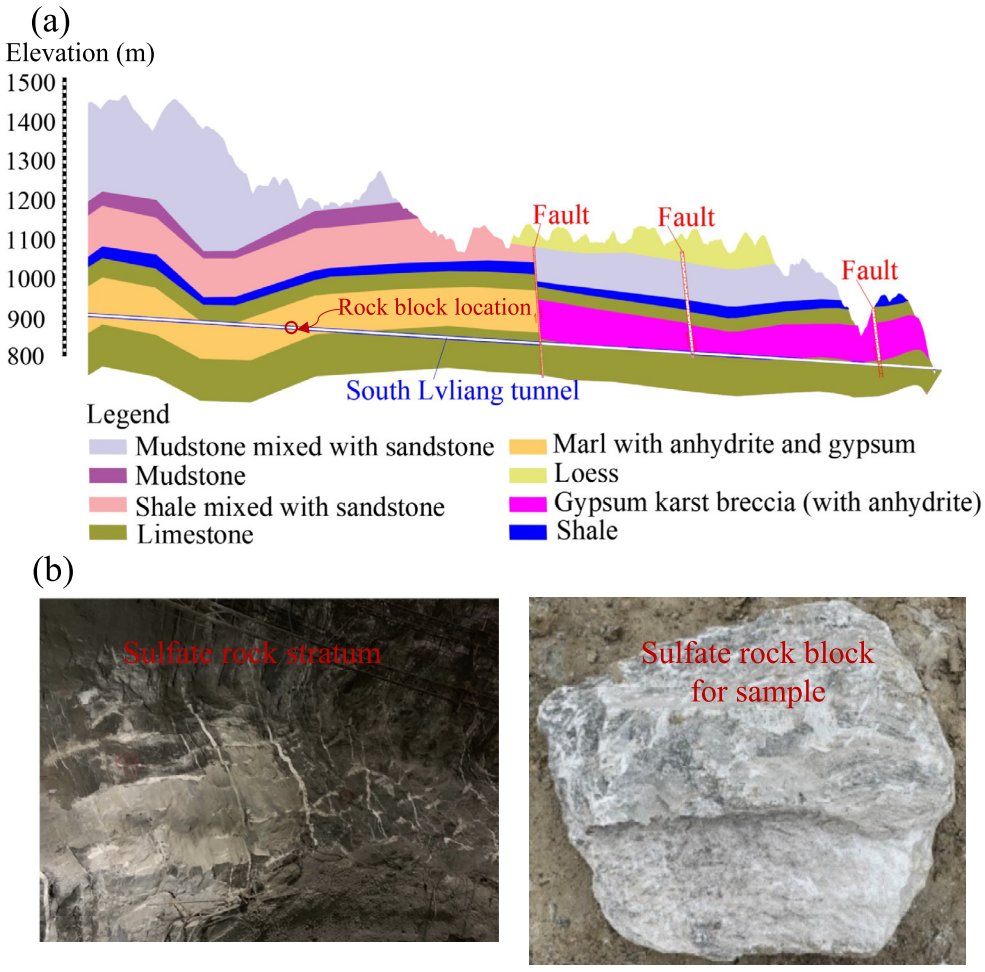

Fig. 2. Location map of the study area. (a) Rock block location of the tunnel, and (b) origin rock block of sample.

The UCS tests were conducted using a TAW-2000 electrohydraulic servo rock triaxial testing machine, as shown in Fig. 6. This apparatus is capable of performing both UCS and triaxial compressive strength tests on rock specimens. The UCS testing procedure adhered to the methodology proposed by Wang et al. (2014). A constant loading rate of 0.001 mm/s was applied during the uniaxial tests. During each test, a transducer recorded the axial load, axial displacement, and radial displacement.

3 DEM numerical simulation

3.1 3DEC-GBM modeling method

Numerical modeling has emerged as a powerful tool to study mechanical behaviors of rock, rock-like materials, and jointed rock masses (Wang & Cai, 2019). Numerical modeling methods, in comparison to experimental approaches, offer significant advantages, especially in observing detailed phenomena like cracks, stress, and strain within specimens. This detailed information is valuable for gaining further insight into failure mechanisms and microscopic failure modes. At the micro-scale, rock materials are composed of grains of different sizes. In numerical modeling, different grain shapes are used to consider rock heterogeneity at the grain scale. For instance, disk and sphere, square and cube, triangular and tetrahedron, and polygonal and polyhedron shapes have been used (Ghazvinian et al., 2014; Kazerani & Zhao, 2010; Wang & Cai, 2019; Zhang et al., 2021).

Currently, 3DEC incorporates two types of grain-based models: the tetrahedron grain model and the polyhedron grain model, the latter utilizing the 3DEC-Voronoi modeling approach, as illustrated in Fig. 7. Grain geometry plays a critical role in the development of crack propagation and sliding fractures. Distinct differences in grain morphology and arrangement between the two models lead to varied mechanical responses. From a geometric standpoint, Voronoi tessellations introduce heterogeneity in grain shape and size, closely resembling actual mineral grain structures. Moreover, Voronoi grains can be configured with various aspect ratios, thereby enhancing the simulation of anisotropic behavior in rock materials (Ghazvinian et al., 2014). In contrast, tetrahedron grains are consistently smooth, four-faced polyhedra that tend to form continuous surfaces, predominantly resulting in shear failure, as illustrated in Fig. 7

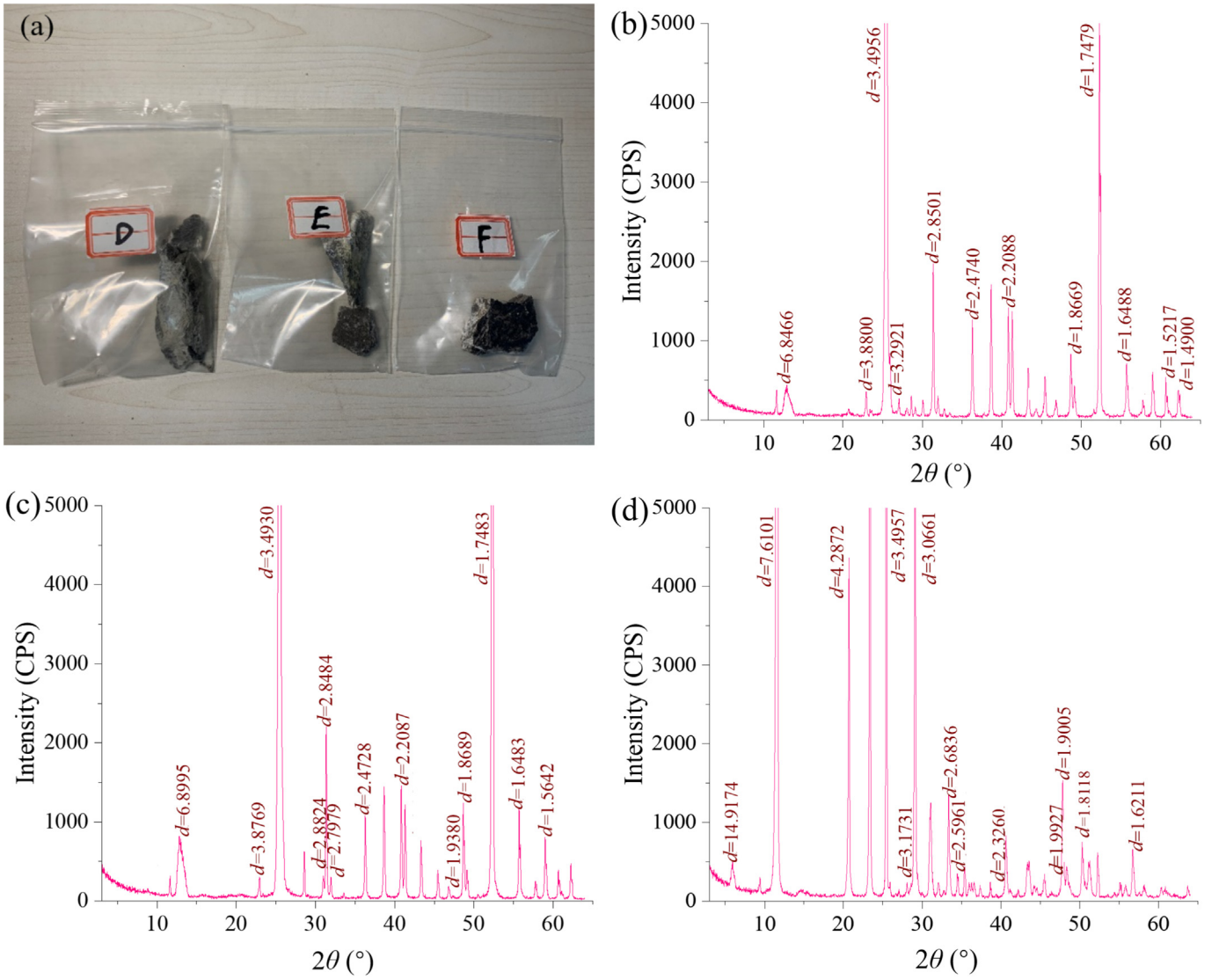

Fig. 3. XRD results of the studied rock blocks. (a) Sample for XRD testing, (b) XRD test results of specimen D, (c) XRD test results of specimen E, and (d) XRD test results of specimen F.

(a) by red lines. Conversely, the rough surfaces of Voronoi grains promote splitting as the dominant failure mode rather than shear, as shown in Fig. 7(b) with blue lines (Ghazvinian et al., 2014; Wang & Cai, 2019).

Voronoi tessellation is one of the available techniques for generating random polygonal grains within a given domain. In this method, random seed points are distributed throughout the region. A 3D Voronoi tessellation is a partition of a domain of $3D$ space, $D \in \mathbb{R}^3$. Given a number of seed points in D, $\{S_i(x_i)\}$ for $i = \{1, \cdots, N\}$, every seed is assigned a Voronoi cell, C_i, as follows (Ghazvinian et al., 2014):

$$C_i = \left\{P(x) \in D | d(P, S_i) \leq d(P, S_j)\ \forall j \neq i\right\}, \tag{2}$$

where $d(\cdot, \cdot)$ is the Euclidean distance. In the Voronoi tessellation algorithm, to construct the cell C_i associated with the seed S_j, the entire computational domain is initially assigned as the preliminary region. This region is iteratively refined by sequentially incorporating the influence of neighboring seeds S_j, ordered by their increasing Euclidean distance from S_i. At each iteration, the current estimate of C_i is updated by intersecting it with the half-space defined as being closer to S_i than to S_j. This refinement continues until the distance between S_i and a given S_j exceeds a threshold, beyond which the corresponding half-space is guaranteed to encompass the entire cell. A simple and isotropic termination criterion is defined as

$$d(S_j, S_i) > 2d_{\max}, \tag{3}$$

$$d_{\max} = \max_{P \in C_i} d(P, S_i) = \max_{P \in \{V_i\}} d(P, S_i), \tag{4}$$

where $\{V_i\}$ is the set of vertices of cell C_i.

The arrangement of tetrahedral grains was generated using a method analogous to Delaunay triangulation (Lee & Schachter, 1980). As in the Voronoi tessellation, a

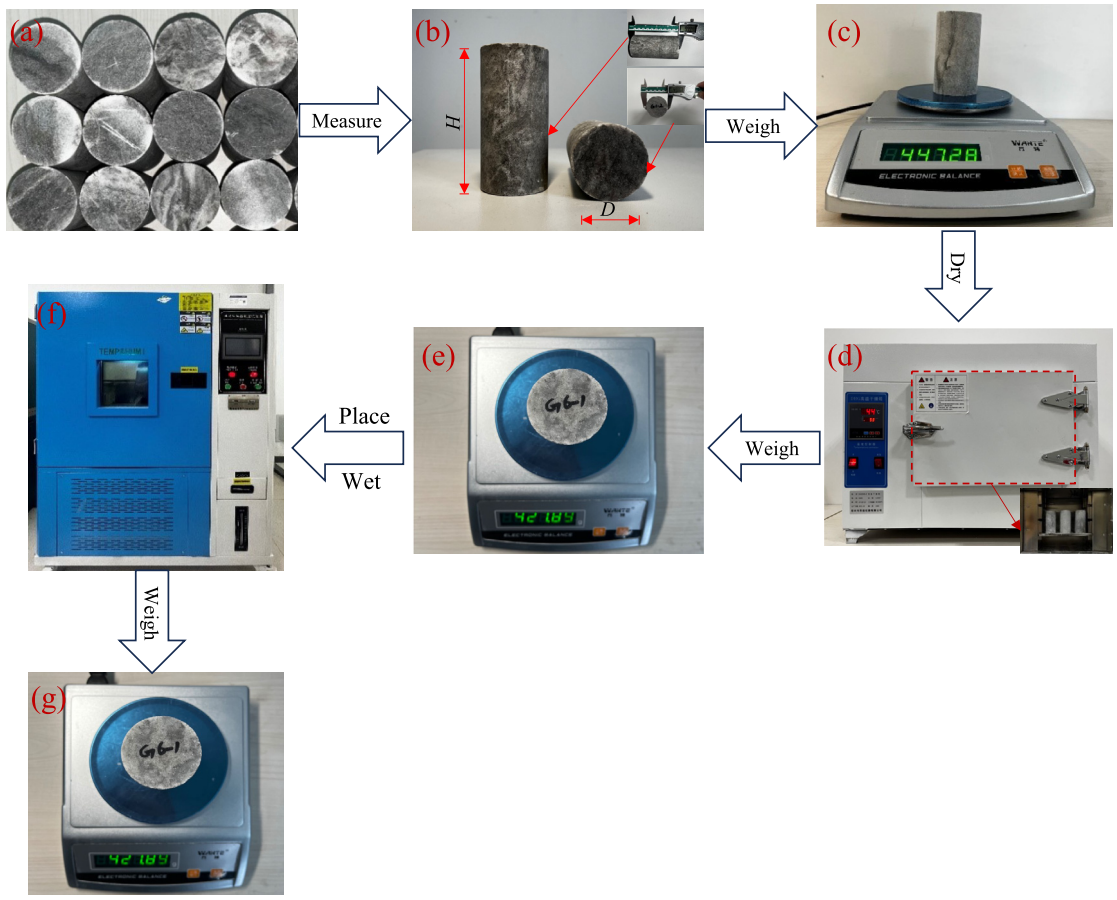

Fig. 4. Preparing process of the testing samples.

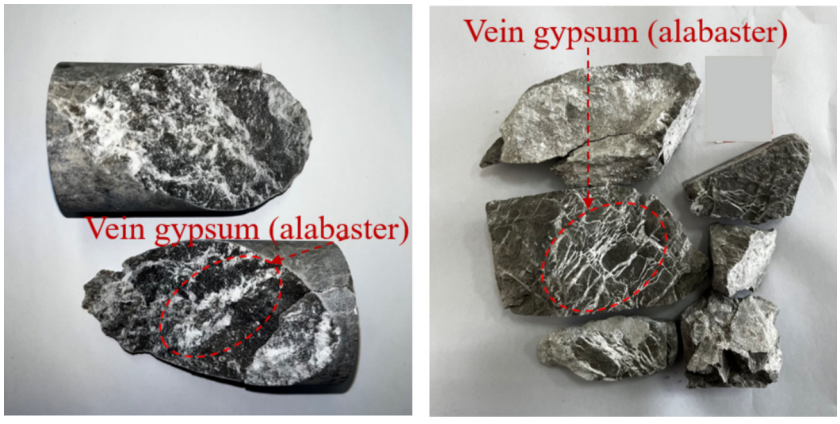

Fig. 5. Gypsum texture of the studied rocks.

Table 1
UCS tests of sulfate rock with different initial water content conditions.

Sample No.	Initial water content (%)
S1	0
S2	3
S3	6
S4	9

set of seed points is defined in an n-D Euclidean space. The Delaunay triangulation creates a set of triangles where no points lie inside the circum-hypersphere of any triangle. Furthermore, Delaunay triangulations maximize the minimum angle of all angles in the triangulation, which works to reduce the number of long, skinny triangles as much as possible (Azocar, 2016).

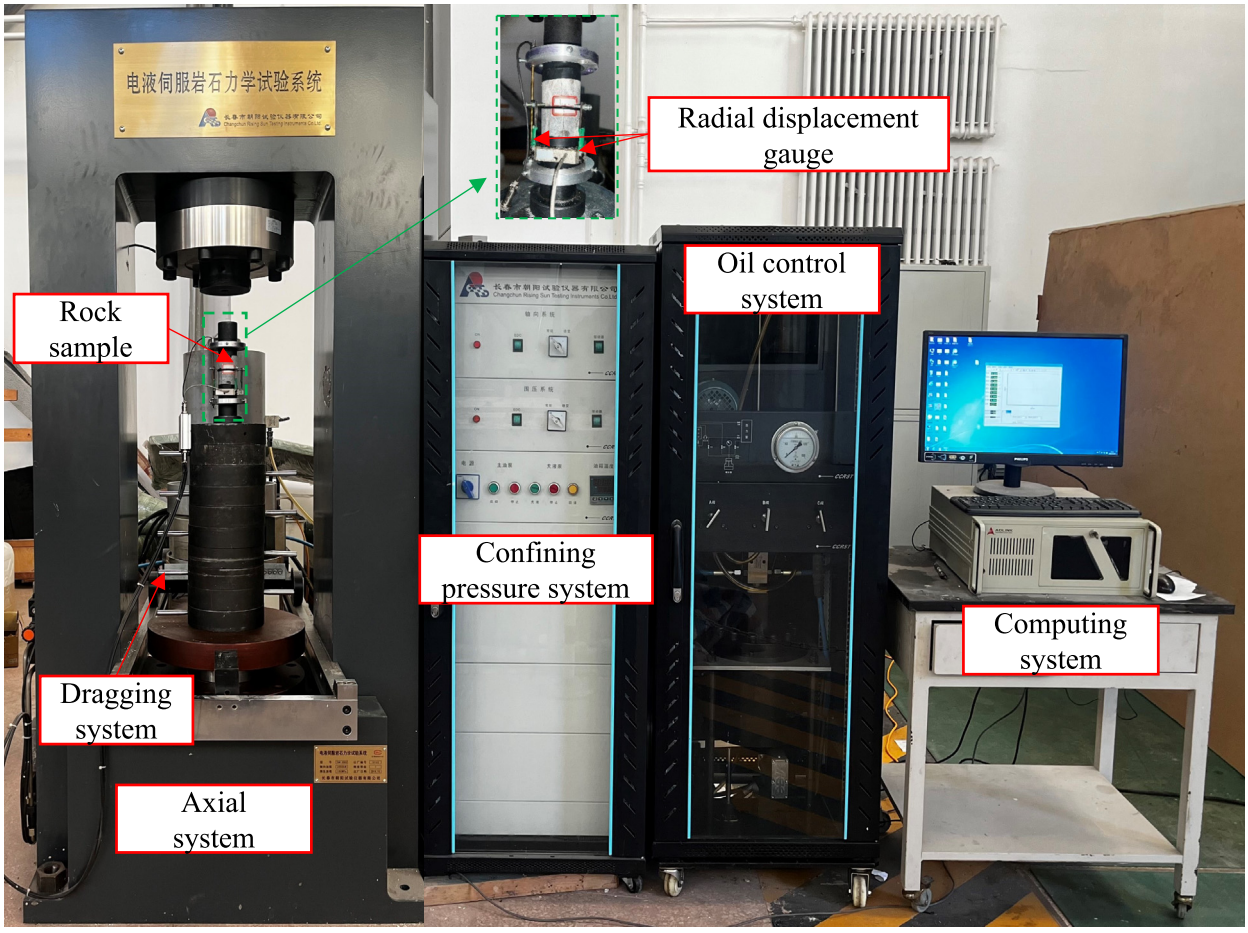

Fig. 6. TAW-2000 electro-hydraulic servo-controlled rock mechanics testing apparatus.

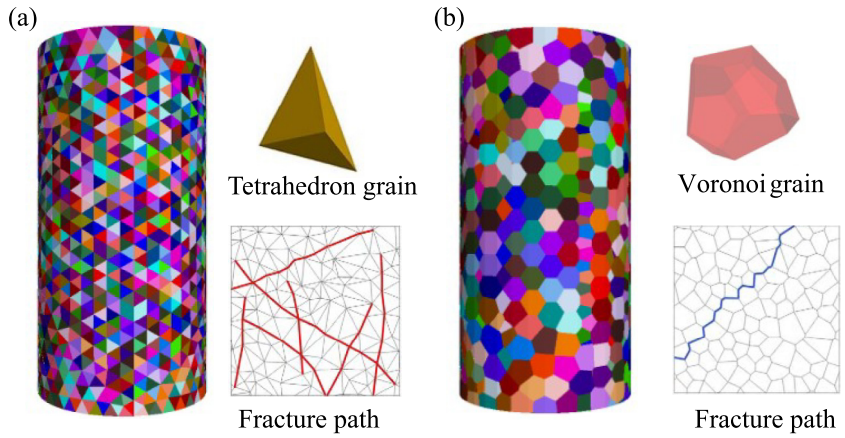

Fig. 7. Comparison of grain shapes and fracture development paths in 3DEC-GBM. (a) Tetrahedron grains generated from 3DEC, and (b) polyhedron grains generated from Voronoi tessellation from 3DEC.

Upon completion of the model construction, inter-grain contacts are automatically generated. The Coulomb-slip model was used for block contacts in this study. In the elastic range, the contact behaviour is governed by the normal (k_n) and shear (k_s) stiffness parameters (Turichshev & Hadjigeorgiou, 2017):

$$\Delta F_n = -k_n \Delta u_n A, \quad (5)$$

$$\Delta F_s = -k_s \Delta u_s A, \quad (6)$$

where ΔF_n and ΔF_s are the increments of normal force (F_n) and shear force (F_s), respectively; Δu_n and Δu_s are the increments of normal displacement and shear displacement, respectively; A is the contact area.

A contact does not fail under compression; rather, it fails in tension once its tensile strength is exceeded (Turichshev & Hadjigeorgiou, 2017). The maximum tensile force (T_{max}) is given by

$$T_{max} = -\sigma_{t\,max} A, \tag{7}$$

where $\sigma_{t\,max}$ is the tensile strength.

According to Coulomb's friction law, the maximum shear force (F_{smax}) that a contact can sustain without slipping is defined.

$$F_{s\,max} = F_n \tan\varphi + cA, \tag{8}$$

where φ and c are the cohesion and friction angles, respectively.

After exceeding the maximum shear force, the contact undergoes slip, during which the tensile strength, cohesion, and friction angle decrease to their respective residual values.

Although Voronoi surface subdivision provides a more realistic representation of grain morphology, it incurs higher computational costs and increases the risk of model instability due to smaller faces and edges. In contrast, despite its geometric simplicity, the tetrahedron grain model is easier to implement in complex mining geometries and produces cleaner shapes with greater computational efficiency (Azocar, 2016). In real rocks, failure may occur through tensile fracturing, shear failure, or a combination of both. A grain-based model composed exclusively of either tetrahedron or Voronoi grains can simulate only a single failure mode, thereby failing to capture the complex fracture mechanisms observed at the microscale. To overcome this limitation, a novel grain-based model is proposed, integrating both tetrahedron and Voronoi grains to leverage the advantages of each configuration. The simulations are performed using 3DEC, a discrete element method (DEM) code developed by Itasca Consulting Group Inc. (2025). Specifically, the model generation process begins by creating a specified number of random Voronoi grains within a defined region using the 3DEC Voronoi modeling approach. Each Voronoi grain is then subdivided into tetrahedral elements, ensuring that the tetrahedra collectively fill the original boundaries of the Voronoi grain, as illustrated in Fig. 8.

3.2 Numerical UCS tests

Numerical experimental models were developed using the new 3DEC-GBM modeling method described in Section 3.1. To minimize the influence of boundary effects on the grain geometry of cylindrical specimens, a three-dimensional cuboid domain measuring 120 mm in height and 60 mm in width was first generated, as illustrated in Fig. 9(a). Cylindrical specimens for UCS testing were then extracted from the center of the tessellated domain, with 10 mm removed from both the top and bottom ends. The resulting specimen had a diameter of 50 mm and a length of 100 mm, as shown in Fig. 9(b). To ensure uniform stress distribution during UCS testing, high-stiffness platens—each 50 mm in diameter and 10 mm in height—were attached to the specimen's top and bottom surfaces, as depicted in Fig. 9(c). Finally, the Voronoi tessellations were further subdivided into smaller cells using the 3DEC command in accordance with the New 3DEC-GBM modeling method, as shown in Fig. 9(d).

The loading of the UCS models was achieved by applying a constant velocity of 0.001 mm/s. This velocity is consistent with laboratory UCS tests and was applied to the top and bottom platens of the specimens. For the specimens under investigation, the axial stress was quantified through a method that averaged the stress across different block zones. This method specifically focused on blocks

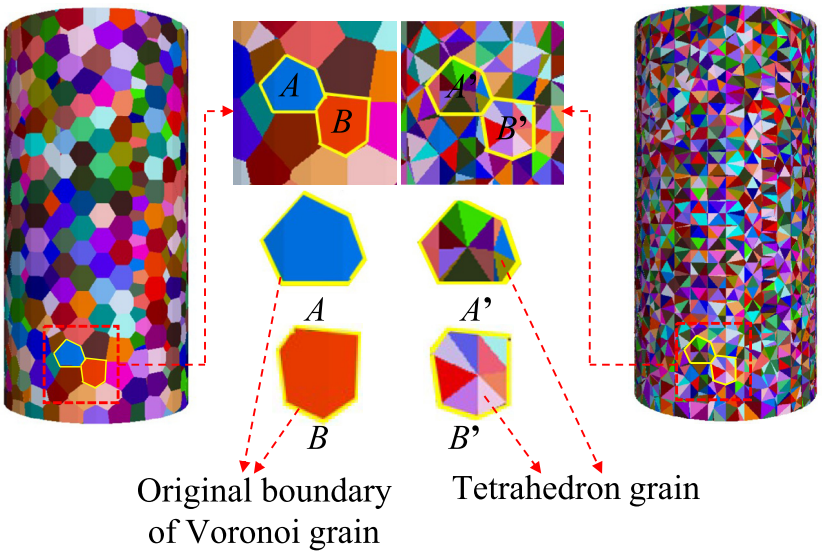

Fig. 8. Modeling process of the new 3DEC-GBM model.

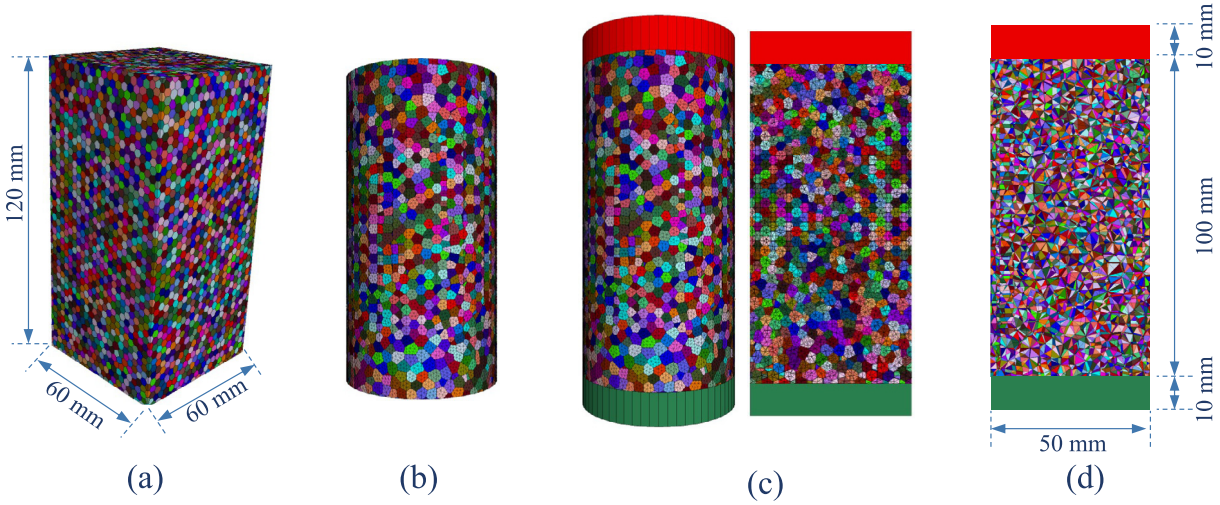

Fig. 9. Numerical specimen model in 3DEC. (a) Generation of a Voronoi tessellation cuboid, (b) cutting the cuboid into a cylindrical specimen, (c) adding platens, and (d) subdividing Voronoi tessellations into tetrahedra.

whose centroids were located within a central cubic region of the cylindrical sample. A box size with dimensions of 35 mm × 35 mm × 40 mm was used to measure axial stress within the specimens, as shown in Fig. 10(a) (Ghazvinian et al., 2014; Kanit et al., 2003). The axial strain of each specimen was determined by averaging the relative displacements between ten pairs of monitoring points located at both ends of the model. These points were spaced 10 mm apart along the axis. The lateral strain was calculated by averaging the relative displacement differences of six pairs of monitoring points. This included three pairs in the *x*-direction and three pairs in the *y*-direction, with each monitoring point spaced 10 mm from its adjacent point on either side and 2 mm from the boundaries of the model, as illustrated in Fig. 10(b).

The correct determination of the calibrated micro-parameters in the GBM model is a prerequisite to ensure the accuracy of numerical simulation results. In DEM simulation, parameter calibration is an essential step to obtain a set of reasonable meso-parameters according to the macro-parameters of a given material. The micro- and macro-mechanical behaviors of 3DEC-GBM models are controlled by two key components: the grains and the contacts (joints) between these grains. Based on previous research findings (Ghazvinian et al., 2014; Kazerani et al., 2010; Wang & Cai, 2019), in this study, an elastic

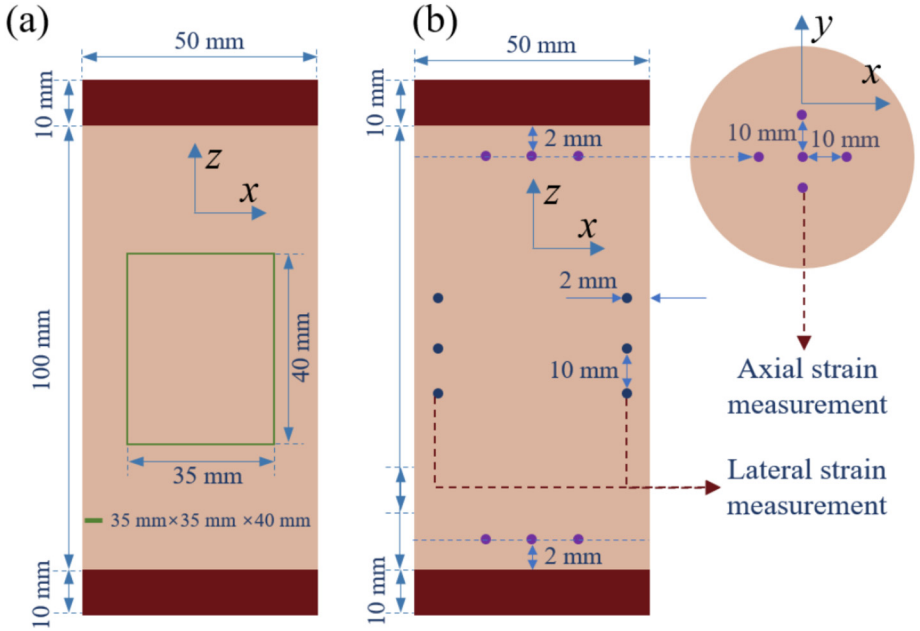

Fig. 10. Monitoring positions for strain and stress measurement in uniaxial compression tests. (a) Box size investigated for axial stress measurement, and (b) location of points for axial and lateral strain measurement.

model and a Coulomb slip joint model are respectively employed for the 3DEC grains and grain contacts. The parameters requiring calibration of an elastic block model of Coulomb slip joint contacts model in 3DEC, are as follows: grain (block) Young's modulus (E), grain (block) Poisson's ratio (v), contact normal stiffness ($J\mathrm{K_n}$), contact shear stiffness ($J\mathrm{K_s}$), contact peak cohesion ($J\mathrm{C_p}$), contact peak friction angle ($J_{\phi p}$), contact peak tensile strength ($J_{\sigma_{TP}}$), contact residual cohesion ($J\mathrm{C_r}$), contact residual friction angle ($J_{\phi r}$), and contact residual tensile strength ($J_{\sigma_{Tr}}$). The fundamental principle of a calibration is that the modeling results should match the material properties obtained from the laboratory test. From a mechanical point of view, the calibrating targets include not only the deformation properties (Young's modulus and Poisson's ratio) but also strength parameters (e.g., peak stress) and the mode of failure. Trial-and-error method can be used to calibrate 3DEC-GBM models (Farahmand et al., 2018; Gao et al., 2016; Wang & Cai, 2018).

Before introducing the calibration procedures, parameter sensitivity analysis is necessary to evaluate the impact of meso-parameters on the macro-properties of materials (Zhang et al., 2023). In DEM simulation, parameter sensitivity analysis was performed (Azocar, 2016; Ghazvinian et al., 2014; Sinha & Walton, 2020; Wang & Cai, 2019; Zhang et al., 2023). Based on previous sensitivity analysis research results, calibration procedures of grain and grain contact parameters for 3DEC-GBM in UCS test were established, as shown in Fig. 11.

4 Results and discussion

4.1 Comparison of laboratory and numerical UCS test results

The UCS results of the sulfate rock specimens are presented in Table 2. As shown in the table, both the UCS and Young's modulus decrease with increasing initial water

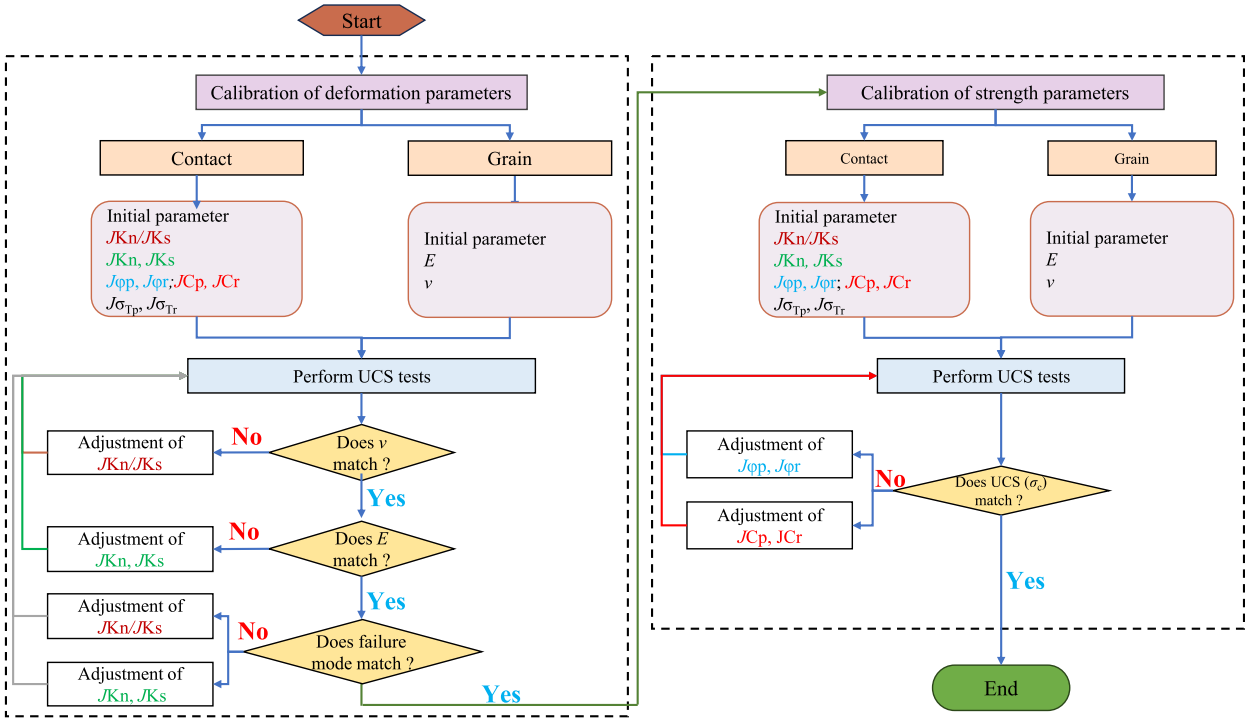

Fig. 11. Schematic diagram of calibration procedures of grain and grain contact parameters for 3DEC-GBM in UCS test.

Table 2
UCS test results of sulfate rock.

Sample No.	Initial water content (%)	UCS (MPa)	Young's modulus (GPa)	Poisson's ratio
S1	0	22.178	7.769	0.10
S2	3	17.195	6.527	0.14
S3	6	14.290	5.127	0.21
S4	9	10.388	3.969	0.39

content, while Poisson's ratio increases under the same condition.

Based on the above calibration procedure, different micro-parameters of GBM were selected, and a series of trial-and-error numerical simulations was conducted. Ultimately, the calibrated grain and grain contact micro-parameters, obtained after repeated trial-and-error, are listed in Table 3. A comparison of the experimental and numerical results of sulfate rock is shown in Fig. 12. According to Fig. 12, the final failure pattern obtained from numerical simulations, based on the micro-parameters of sulfate rock listed in Table 3, is consistent with the failure mode observed in laboratory experiments.

A comparison of the macroscopic deformation and strength properties (i.e., Young's modulus, Poisson's ratio, peak stress) between sulfate rock and four modeling cases is presented in Fig. 12. In this study, Young's modulus refers to the slope of the elastic portion of the stress–strain curve, i.e., the tangential elastic modulus. Poisson's ratio is defined as the absolute value of lateral strain divided by axial strain during the elastic deformation phase. As shown in Fig. 13, the absolute error between the Young's modulus obtained from numerical simulations and that from laboratory experiments ranges from 0.89% to 2.6%. For sulfate rock with an initial water content of 0, the Poisson's ratio derived from numerical simulations matches the experimental value. For initial water content of 3%, 6%, and 9%, the absolute error in Poisson's ratio ranges from 1.28% to 2.38%. Additionally, the absolute error in peak stress between the numerical and experimental results ranges from 0.09% to 2.02%. These findings demonstrate good agreement between the numerical simulations and laboratory experiments.

Using the specimen with an initial water content of 9% as an example, a comparison was conducted between the simulation results of the 3DEC-GBM model, the Voronoi grains model, and the tetrahedral grains model, relative to the experimental results, as shown in Fig. 14. Under otherwise identical conditions, the relative errors in uniaxial compressive strength for the 3DEC-GBM, Voronoi, and tetrahedral grains models were 0.31%, 2.45%, and 3.94%, respectively. The corresponding errors in elastic modulus were 2.6%, 4.43%, and 3.6%, while those for Poisson's ratio were 1.28%, 2.05%, and 5.64%, respectively. These results demonstrate that the 3DEC-GBM model provides higher accuracy in mechanical parameter inversion compared to both the standalone Voronoi and tetrahedral grains models.

The simulations were performed using 3DEC version 9.0 (Itasca Consulting Group Inc., 2025), on a system equipped with a 13th Gen Intel i7-13700KF CPU, 32 GB DDR5 4800 MHz RAM, and an NVIDIA GeForce RTX 3060 Ti GPU. Under identical modeling conditions, the computation time for a single specimen was 15 h for the Voronoi grain model, 8.2 h for the tetrahedral model, and 9.1 h for the proposed 3DEC-GBM model. In summary, the 3DEC-GBM model enhances simulation accuracy while also improving computational efficiency, making it particularly advantageous for DEM simulations involving iterative meso-parameter calibration and large-scale engineering analyses.

4.2 Influence of initial water content on deformation properties

The relationships between Young's modulus and Poisson's ratio of sulfate rock with respect to initial water content are presented in Fig. 15(a) and (b), respectively. These results indicate that the macroscopic deformation properties are strongly influenced by the rock's initial water content. As shown in Fig. 15(a), Young's modulus decreases progressively with increasing water content, although the rate of decrease diminishes at higher water content. The relationship between Young's modulus and initial water content observed in this study can be expressed by the following fitting equation:

$$E(w_i) = m_1 \cdot \exp(n_1 \cdot w_i), \tag{9}$$

where $E(w_i)$ represents the Young's modulus at an initial water content of w_i; m_1 and n_1 are constants. In this test,

Table 3
Calibrated grain and contact property micro-parameters of sulfate rock with different initial water content (w_i).

Type	Property		Value			
			$w_i = 0$	$w_i = 3\%$	$w_i = 6\%$	$w_i = 9\%$
Grainparameters	Density	ρ (kg/m^3)	2348	2355	2480	2560
	Young's modulus	E (GPa)	4.8	4.0	3.25	3.0
	Poisson's ratio	v	0.17	0.22	0.26	0.31
Contactparameters	Normal stiffness	JK_n (GPa/m)	1420	1020	821	576
	Shear stiffness	JK_s (GPa/m)	568	470	323	230.4
	Peak cohesion	JC_p (MPa)	11.2	9.26	7.8	6.6
	Peak friction angle	$J_{\phi p}$ (°)	27	25.4	23.8	23
	Peak tensile strength	$J_{\sigma_{Tp}}$ (MPa)	4.48	3.5	2.7	2.0
	Residual cohesion	JC_r (MPa)	0	0	0	0
	Residual friction angle	$J_{\phi r}$ (°)	11	9.1	8.4	8
	Residual tensile strength	$J_{\sigma_{Tr}}$ (MPa)	0	0	0	0

Note: Contacts residual cohesion and residual tensile strength are assumed to be zero (Ghazvinian et al., 2014; Kazerani et al., 2010; Wang & Cai, 2019).

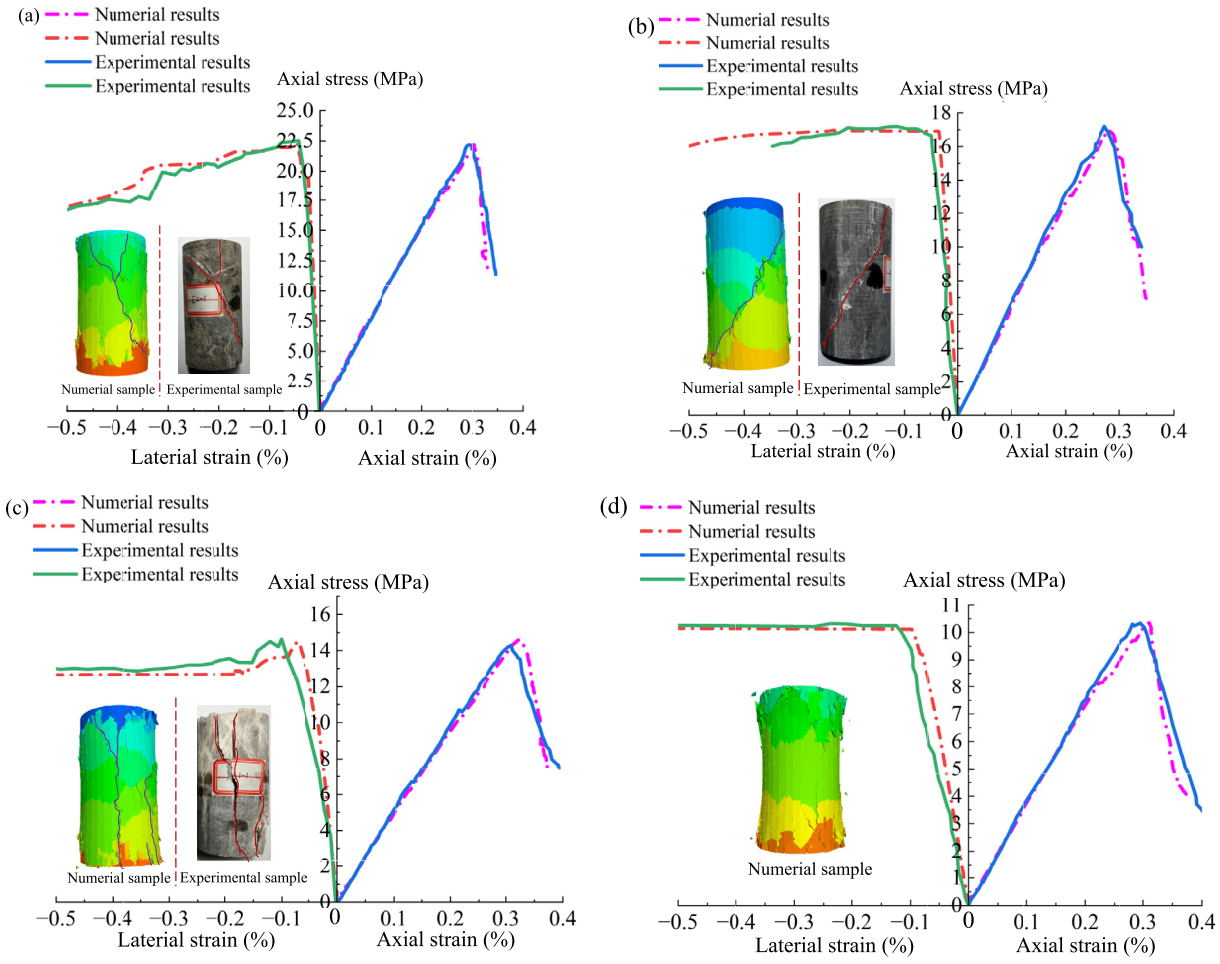

Fig. 12. Comparison between modeling and experimental results of unconfined compression failure pattern for sulfate rock with different initial water content: (a) $w_i = 0$, (b) $w_i = 3\%$, (c) $w_i = 6\%$, and (d) $w_i = 9\%$. Note: The sample with an initial water content of 0 broke during the UCS test, resulting in the absence of pictures for this sample.

the values of m_1 and n_1 are 7.879 and −0.073, respectively. The correlation coefficient squared (R^2) of the fitted line is 0.992, as shown in Fig. 15(a). The parameter m_1 denotes the Young's modulus when the initial water content is 0. The parameter n_1 indicates the decreasing rate of Young's modulus with increasing initial water content.

Figure 15(b) shows that as the initial water content increases, the Poisson's ratio of the rock gradually increases. The relationship between the Poisson's ratio and initial water content in this test can be fitted by the following equation:

$$v(w_i) = m_2 \cdot \exp(n_2 \cdot w_i), \tag{10}$$

where $v(w_i)$ represents the Poisson's ratio at an initial water content w_i; m_2 and n_2 are constants. In this test, the values of m_2 and n_2 are 0.083 and 0.169, respectively. The correlation coefficient squared (R^2) of the fitted line is 0.9851, as shown in Fig. 15(b). The parameter m_2 denotes the Poisson's ratio when the initial water content is 0. The parameter n_2 indicates the increasing rate of Poisson's ratio with increasing initial water content.

The influence of initial water content on Young's modulus and Poisson's ratio can be explained from the perspective of rock damage. The degree of damage to the rock can be evaluated by the damage variable. According to Lemaitre's strain equivalence principle and the concept of effective stress, the damage variable D_v is defined based on the Young's modulus (Lemaitre, 2013).

$$D_v(w_i) = 1 - \frac{E(w_i)}{E(0)}, \tag{11}$$

where $D_v(w_i)$ represents the damage variable of sulfate rock due to water absorption, and $E(w_i)$ represents the Young's modulus at an initial water content of w_i; $E(0)$ represents sulfate rock that does not absorb water, i.e., m_1.

Substituting Eq. (9) into Eq. (11) yields the damage evolution for sulfate rock as

$$D_v(w_i) = 1 - \exp(n_1 \cdot w_i). \tag{12}$$

In this test, the value of n_1 is −0.073.

If the stress–strain curve of the rock is obtained from experiments, the damage variable can also be expressed in the following equation (He & Ahrens, 1994):

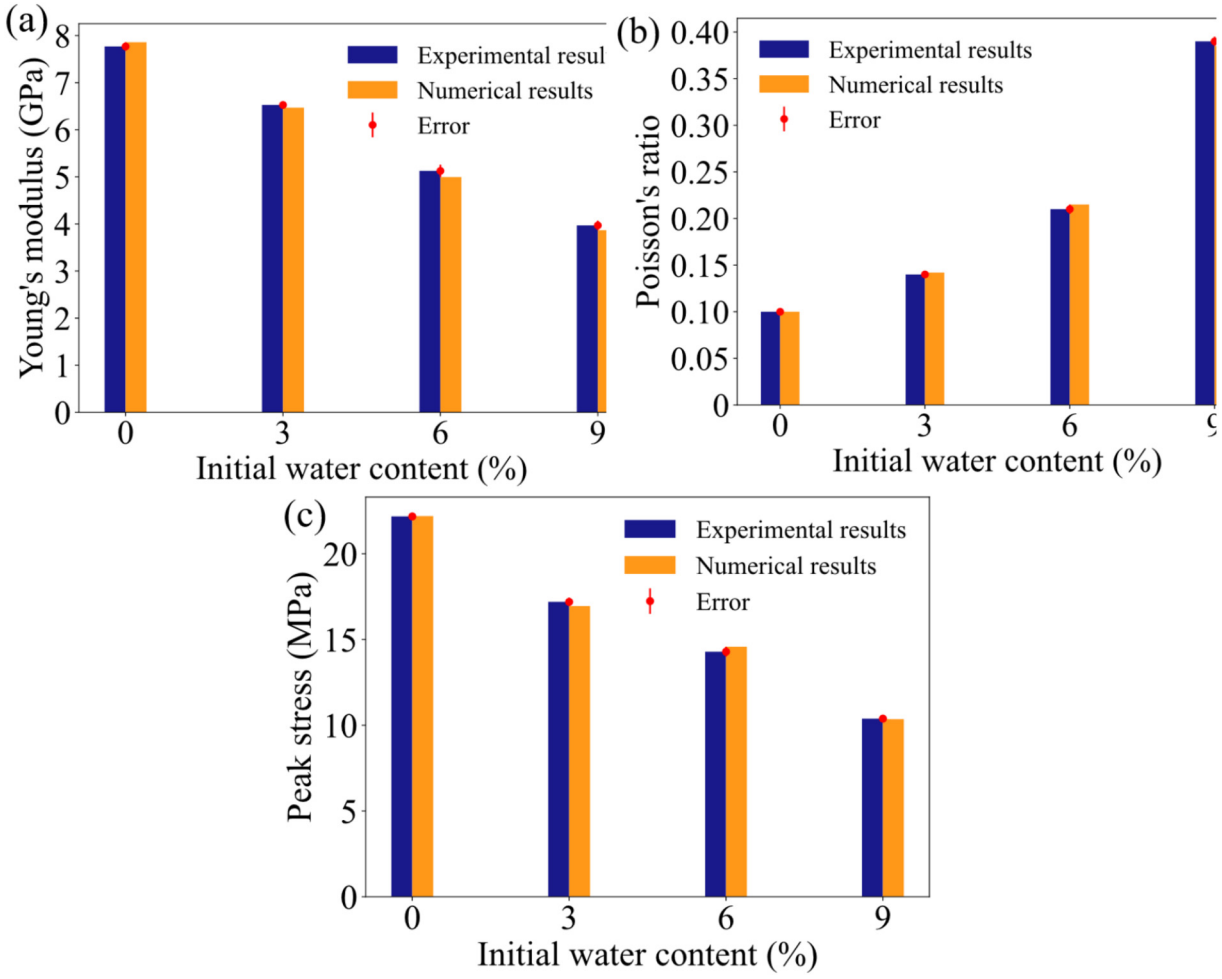

Fig. 13. Errors in deformation and mechanical properties obtained from numerical simulations and laboratory tests. (a) Young's modulus errors, (b) Poisson's ratio errors, and (c) peak stress (UCS) errors.

$$D_{\mathrm{v}}(w_{\mathrm{i}}) = \left(\varepsilon_{w_{\mathrm{i}}}/\varepsilon_{\mathrm{s}}\right)^{n_3}, \tag{13}$$

where $\varepsilon_{w_{\mathrm{i}}}$ represents axial strain; ε_{s} is constant; n_3 is the brittleness coefficient, where a larger value of n_3 indicates a more brittle material.

The uniaxial stress–strain relationship of rock considering damage is represented by the following equation (Yang et al., 2001):

$$\begin{aligned}\sigma(w_{\mathrm{i}}) &= E(w_{\mathrm{i}})[1 - D_{\mathrm{v}}(w_{\mathrm{i}})]\varepsilon_{w_{\mathrm{i}}} \\ &= E(w_{\mathrm{i}})\left[1 - \left(\varepsilon_{w_{\mathrm{i}}}/\varepsilon_{\mathrm{s}}\right)^{n_3}\right]\varepsilon_{w_{\mathrm{i}}}.\end{aligned} \tag{14}$$

Deriving Eq. (14) leads to the following expression:

$$\frac{\mathrm{d}\sigma(w_{\mathrm{i}})}{\mathrm{d}\varepsilon_{w_{\mathrm{i}}}} = E(w_{\mathrm{i}})\left[1 - (1+n)\frac{\varepsilon_{w_{\mathrm{i}}}^{n_3}}{\varepsilon_{\mathrm{s}}^{n_3}}\right]. \tag{15}$$

The parameters ε_{s} and n can be determined from the peak point $P(\varepsilon_P, \sigma_P)$ of the stress–strain curve of UCS test of the material.

$$\frac{\mathrm{d}\sigma(w_{\mathrm{i}})|_P}{\mathrm{d}\varepsilon_{w_{\mathrm{i}}}|_P} = 0 \tag{16}$$

Substituting Eq. (16) into Eq. (15) yields Eq. (17):

$$\left(\frac{\varepsilon_P}{\varepsilon_{\mathrm{s}}}\right) = \frac{1}{1+n_3}. \tag{17}$$

By substituting Eq. (17) and $(\varepsilon_P, \sigma_P)$ along with Eq. (12) into Eq. (14), the coefficient n_3 can be solved as follows:

$$n_3 = \frac{\mathrm{e}^{n_1 \cdot w_{\mathrm{i}}}}{1 - \mathrm{e}^{n_1 \cdot w_{\mathrm{i}}}}. \tag{18}$$

According to the experimental results and Eqs. (9), (10), (12), and (18), the damage variable, and brittleness coefficient of sulfate rock under different initial water content can be obtained, as shown in Table 4. Based on Table 4, it is evident that the damage variable increases with the increase in initial water content, demonstrating that the water absorption results in internal damage to the rock. Simultaneously, the brittleness coefficient decreases with the increase in initial water content, indicating that water absorption leads to a gradual transition of the rock from brittleness to ductility. This suggests that water absorption causes the sulfate rock to gradually soften. Therefore, the

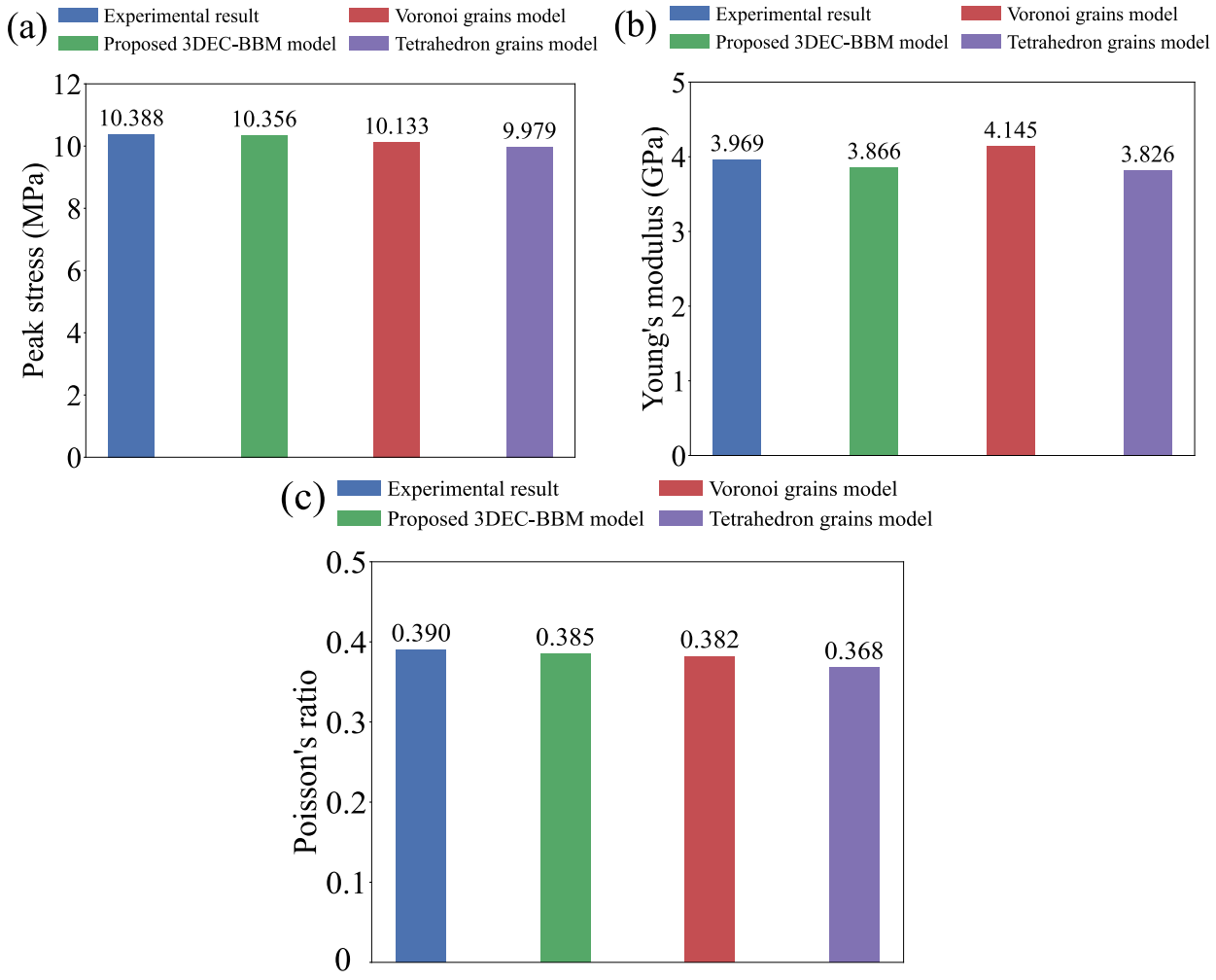

Fig. 14. Comparison of experimental results with numerical results from the proposed 3DEC-BBM model, Voronoi grains model, and tetrahedron grains model. (a) Peak stress, (b) Young's modulus, and (c) Poisson's ratio.

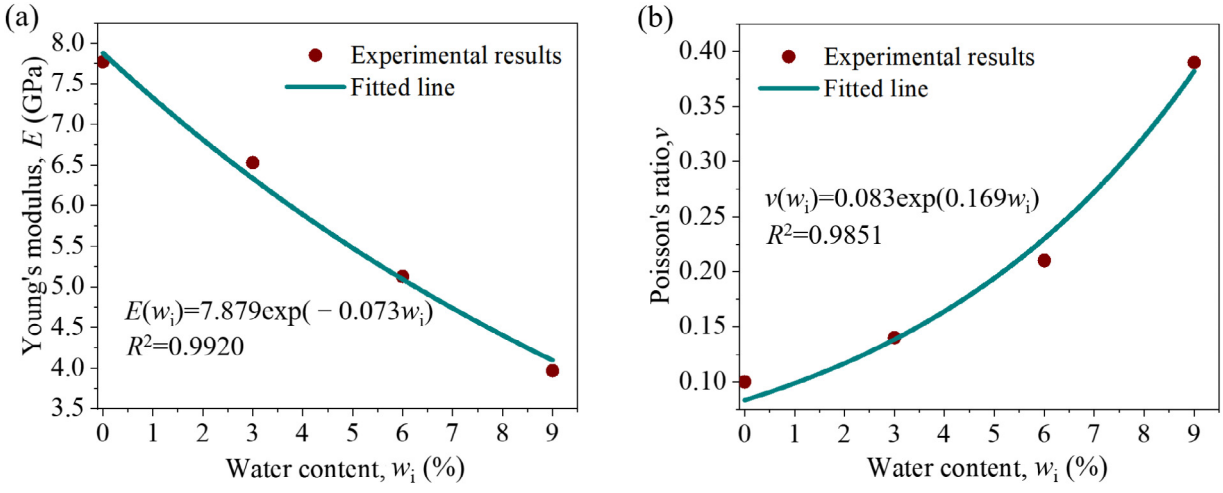

Fig. 15. Variation of Young's modulus and Poisson's ratio with initial water content in UCS tests. (a) Relationship between Young's modulus and initial water content, and (b) relationship between Poisson's ratio and initial water content.

Table 4
Comparison of the damage coefficient and brittleness coefficient of sulfate rock under different initial water content.

Initial water content (%)	0	3	6	9
D_v	0	0.20	0.35	0.48
n_3	–	4.08	1.82	1.08

damage to the rock after water absorption is the fundamental reason for the decrease in Young's modulus and increase in Poisson's ratio of sulfate rock. This damage is caused by the destruction of the internal structure of the rock caused by the combination of water and swelling after absorbing water. Ultimately, as the initial water content increases, the Young's modulus decreases, Poisson's ratio increases, and the deformation of the rock amplifies.

4.3 Influence of initial water content on characteristic stresses

In the investigation of the evolutionary process of rock failure, three important characteristic stress thresholds (i.e., crack initiation stress σ_{ci}, crack damage stress σ_{cd}, and peak strength UCS) have been identified through analysis of laboratory compression test findings (Nicksiar et al., 2012; Zhao et al., 2015). Based on the findings of this literature, a method that integrates the total volumetric strain with the cumulative number of cracks has been systematically adopted for the accurate estimation of characteristic stresses (Ghazvinian et al., 2014; Wang & Cai, 2019; Wang & Cai, 2018).

The mechanical behavior of the numerical sulfate rock model with different initial water content under uniaxial compression is presented in Fig. 16. Taking Fig. 16(a) as an example, the method for determining the characteristic stresses based on numerical simulation results is illustrated. Firstly, σ_{ci} is determined by observing the tangential line that marks a sharp increase in the cumulative shear crack number, as shown by the red curve. A FISH script is used to count the number of shear failure cracks. Secondly, σ_{cd} is estimated from the total volumetric strain curve, specifically at the point corresponding to the reversal point on the pink curve for volumetric strain. This estimation also involves identifying a rapid increase in the number of cumulative tensile cracks, indicated by the light green curve. Thirdly, UCS is determined from the peak of the axial stress–axial strain curve, represented by the blue line. The characteristic stresses derived from Fig. 16 are summarized in Table 5. According to Table 5, the stress thresholds for crack initiation in sulfate rock with initial water content of 0, 3%, 6%, and 9% are 5.109, 4.203, 3.894, and 1.922 MPa, respectively. Similarly, the stress thresholds for crack damage at these initial water contents are 19.969, 16.337, 13.590, and 9.694 MPa, respectively. Lastly, the peak strength stress thresholds for the same initial water content are 22.179, 16.952, 14.578, and 10.356 MPa, respectively.

Table 5
Characteristic stresses of sulfate rock with different initial water content.

Initial water content (%)	0	3	6	9
σ_{ci} (MPa)	5.109	4.203	3.894	1.922
σ_{cd} (MPa)	19.969	16.337	13.590	9.694
UCS (MPa)	22.179	16.952	14.578	10.356

Based on the experimental results in Table 5, the relationship between initial water content and various characteristic stresses, i.e., σ_{ci}, σ_{cd}, and UCS, is modeled as shown in Fig. 17. It can be seen from Fig. 17 that the characteristic stresses decrease as the initial water content of the sulfate rock increases. Moreover, the relationship between characteristic stresses and initial water content is linear. The minimum correlation coefficient (R^2) of the fitting relationship curve is 0.9003, indicating that the mathematical model in Fig. 17 can be used to estimate the characteristic stresses of sulfate rock at different initial water content.

4.4 Influence of initial water content on meso-mechanical properties

Grain and grain contact, which control the micro-mechanical behaviors and consequently the macro-mechanical behavior of a synthetic rock specimen, are the two key components in 3DEC-GBM simulations. It is seen from Fig. 18 that the Young's modulus of grain decreases with the increase of rock initial water content. Conversely, the Poisson's ratio of grain increases with the increase of rock initial water content. When the initial water content of the rock increases from 0 to 3%, 6%, and 9%, the Young's modulus of the grain decreases by 20%, 47.69%, and 60%, respectively, while the Poisson's ratio increases by 22.73%, 34.62%, and 45.16%, respectively. It can be seen that the initial water content has a significant impact on the meso-mechanical properties of the grain in sulfate rock.

The strengths of grain contact control directly the overall strength of the model and the post-peak deformation behavior (Wang & Cai, 2019). Figure 19(a) to (f) shows the influence of rock initial water content on the meso-mechanical parameters of grain contact. As shown in Fig. 19(a), with the initial water content of the rock increasing from 0 to 3%, 6%, and 9%, the normal stiffness of the contact decreases by 39.22%, 72.96%, and 146.53% respectively. Similar trends are observed for other contact meso-mechanical parameters, whereby the meso-mechanical parameters of contact decrease as the initial water content increases. Specifically, when the rock's initial water content increases from 0 to 9%, reductions in the contact's shear stiffness, peak cohesion, peak friction angle, peak tensile strength, and residual friction angle reach 146.54%, 69.70%, 17.39%, 124%, and 37.5% respectively, as shown in Fig. 19(b) to (f). The contact's normal stiffness, shear stiffness, and peak tensile strength are known to be highly sensitive to changes in initial water content. Previous studies (e.g., Fig. 11) have shown that normal and shear stiffness significantly impact the elastic modulus,

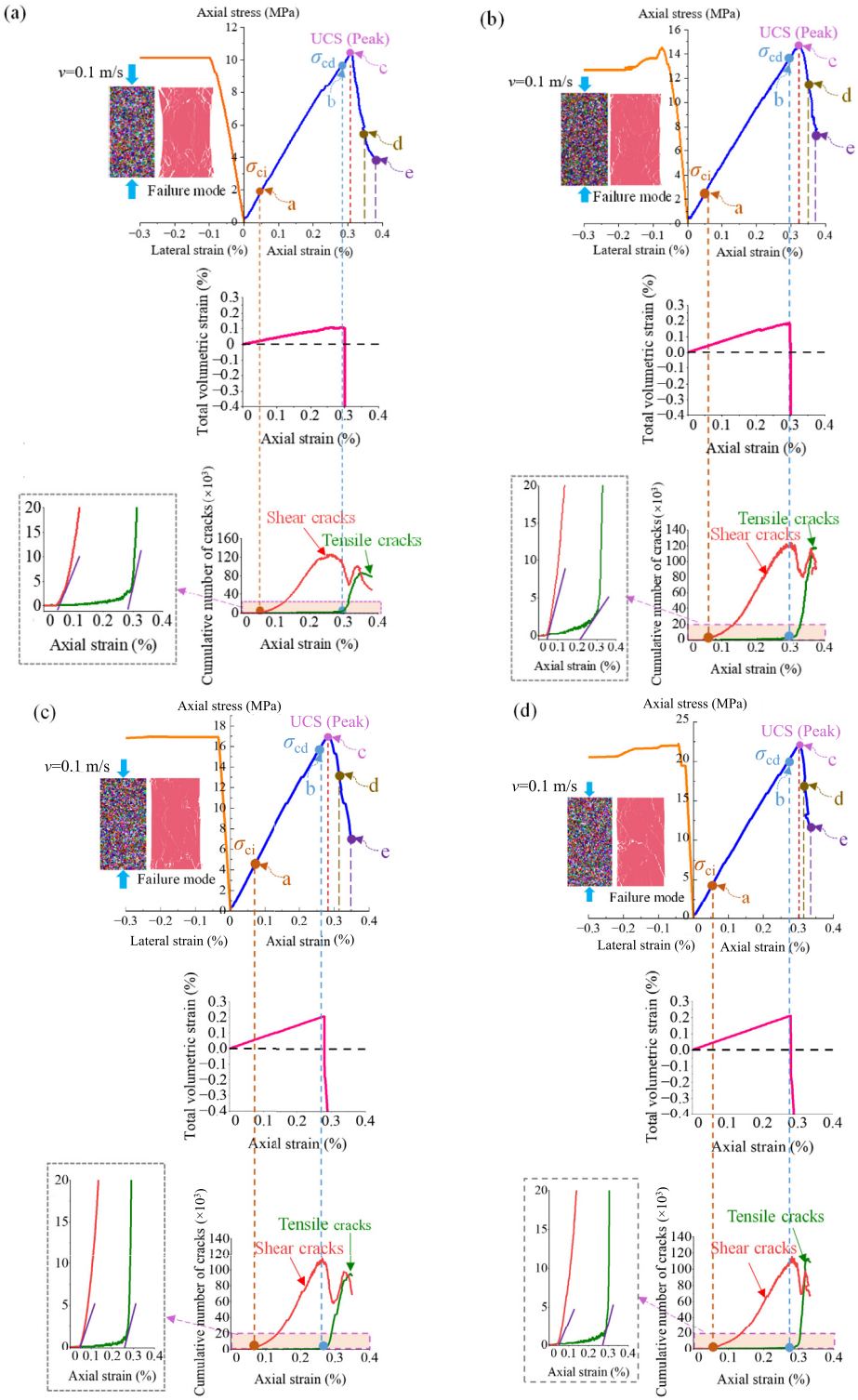

Fig. 16. Modeling curves of axial stress-axial strain, axial stress-lateral strain, and total volumetric strain associated with the cumulative number of tensile and shear cracks for the calibrated UCS test. (a) The initial water content of the numerical specimen is 9%, (b) the initial water content of the numerical specimen is 6%, (c) the initial water content of the numerical specimen is 3%, and (d) the initial water content of the numerical specimen is 0.

Poisson's ratio, and failure mode of rock. It is indicated that the elastic modulus, Poisson's ratio, and failure mode of rock are also highly sensitive to changes in initial water content. Additionally, the peak cohesion, peak friction angle, and residual friction angle of the rock are sensitive to initial water content variations; hence, the uniaxial compressive strength of rock is similarly sensitive to changes in initial water content.

4.5 Influence of initial water content on failure mode

The evolution of grain failure in terms of micro tensile and shear failures and macroscopic fracture patterns at different stages is presented in Fig. 20. Figure 20(a) shows that some micro tensile cracks and shear cracks are randomly distributed throughout the model at the stress level of σ_{ci}. The total number of cracks decreases as the initial water content of sulfate rock increases at the stress level of σ_{ci}. This is consistent with the finding that increasing initial water content reduces σ_{ci}. As shown in Fig. 20(b) and (c), in the phase between the stress level just after σ_{cd} and before reaching UCS, micro shear fractures develop rapidly while micro tensile fractures evolve more slowly. At this stage, macroscopic fractures are almost unobservable. After the stress exceeds UCS, the number of both types of fractures increases rapidly, and the proportion of micro tensile fractures in the total significantly increases. Meanwhile, as shown in Fig. 20(d) and (e), it can be observed that the proportion of micro tensile fractures in the total number of fractures increases with the increase in initial water content.

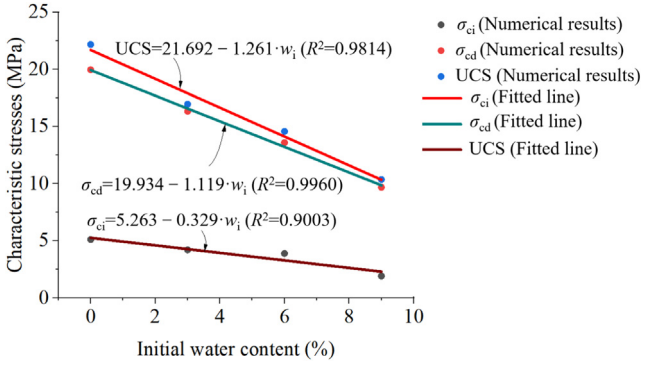

Fig. 17. Relationship between the characteristic stresses of sulfate rock and its initial water content.

On the other hand, based on the orientation, spatial distribution, and morphological characteristics of the macroscopic fractures, it is possible to distinguish between tensile fractures (aligned parallel to the direction of loading, characterized by grain separation) and shear fractures (oriented at an angle to the direction of loading, marked by grain displacement). At the peak, the final failure mode and fracture pattern cannot be clearly identified in UCS tests but can be examined at the post-peak deformation stage. As evidenced by Fig. 20(c), subsequent to attaining peak strength, a significant propagation of tensile and shear fractures within sulfate rock is observed. At the post-peak deformation stage, as shown in Fig. 20(d) and (e) and Fig. 21, in the case where the initial water content of the specimen is zero, the predominant macro failure mode of the specimen is characterized by shear fractures (oriented at an angle to the direction of loading), accompanied by a few non-through-going vertical tensile fractures and some minor sub-vertical tensile fractures (parallel or sub-parallel to the loading direction). In comparison to the specimen with an initial water content of 0, the one with a 3% initial water content exhibits an increase in macro tensile fractures, which are principally developed in the middle height of the simulation model. At an initial water content of 6% for the specimen, there is a decrease in the proportion of macro shear fractures, with macro tensile fractures primarily distributed at both ends and the middle of the specimen. When the initial water content of the specimen is 9%, there is a higher proportion of macro tensile fractures in the specimen, with a small number of shear fractures distributed at both ends. Although axial tensile fractures are the primary macro fractures, the ultimate failure pattern reveals a combination of tensile and shear fractures due to the merging of various types of fractures during the post-peak deformation phase. The macro failure modes observed in the aforementioned models also align with the macro failure patterns of the specimens derived from the experimental results presented in Fig. 12. The above study suggests that

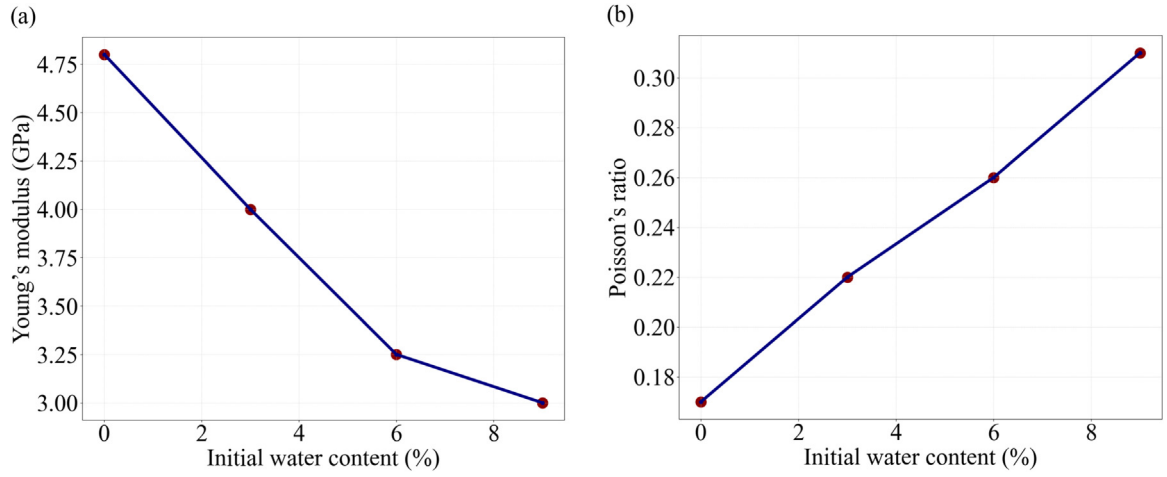

Fig. 18. Grain meso-mechanical parameters: (a) Young's modulus, and (b) Poisson's ratio.

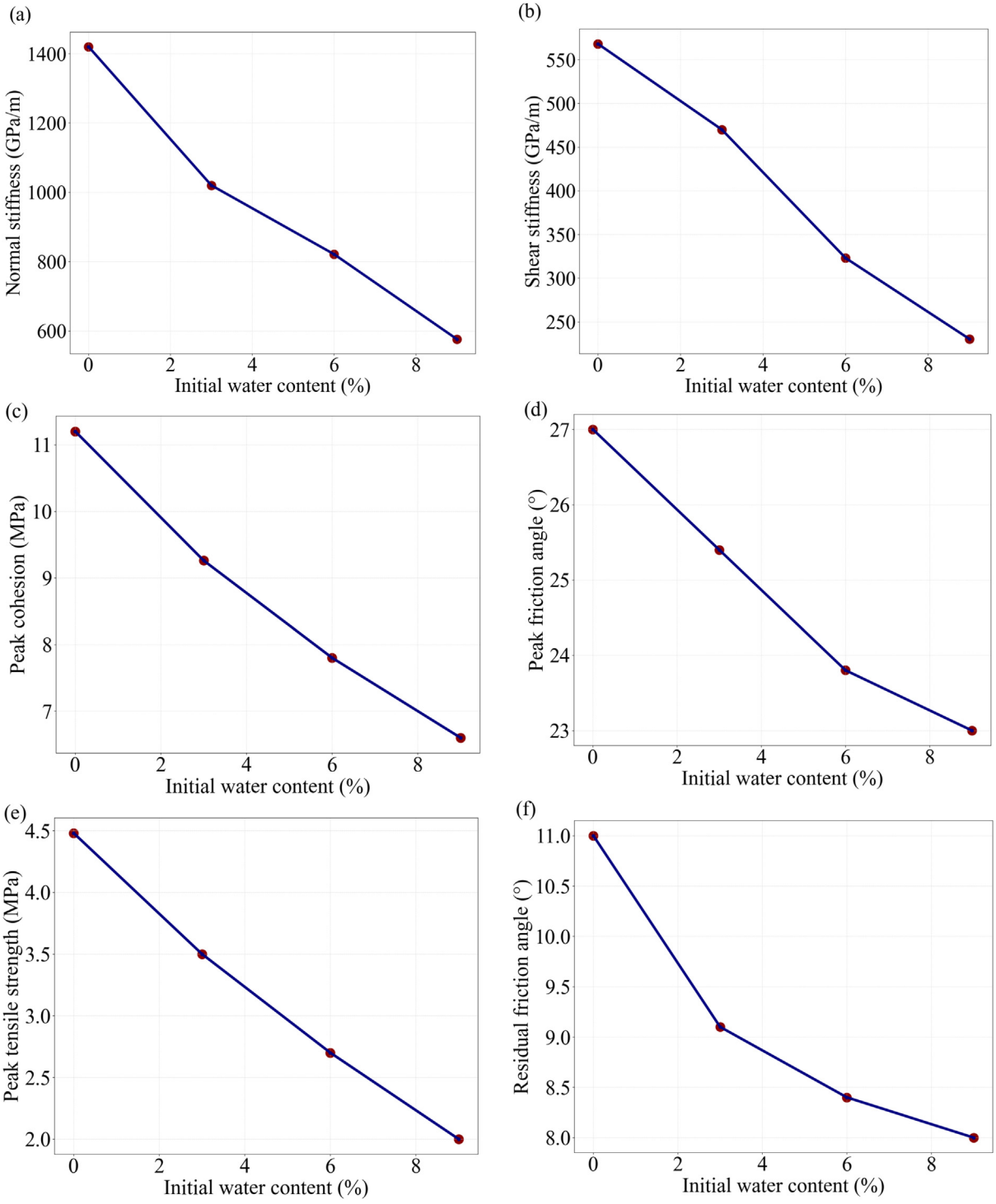

Fig. 19. Contact meso-mechanical parameters: (a) normal stiffness, (b) shear stiffness, (c) peak cohesion, (d) peak friction angle, (e) peak tensile strength, and (f) residual friction angle.

the initial water content of sulfate rock has a large influence on its fracture modes and thus the final pattern. It is proved that as the initial water content increases, the dominant failure mode of sulfate rock gradually transitions from shear to tensile failure. At an initial water content of 6%, the number of tensile cracks in the sulfate rock was 1.71 times that of shear cracks, indicating that tensile failure was dominant. This suggests that 6% water content may serve as a critical threshold, marking the transition from shear-dominated to tensile-dominated failure behavior.

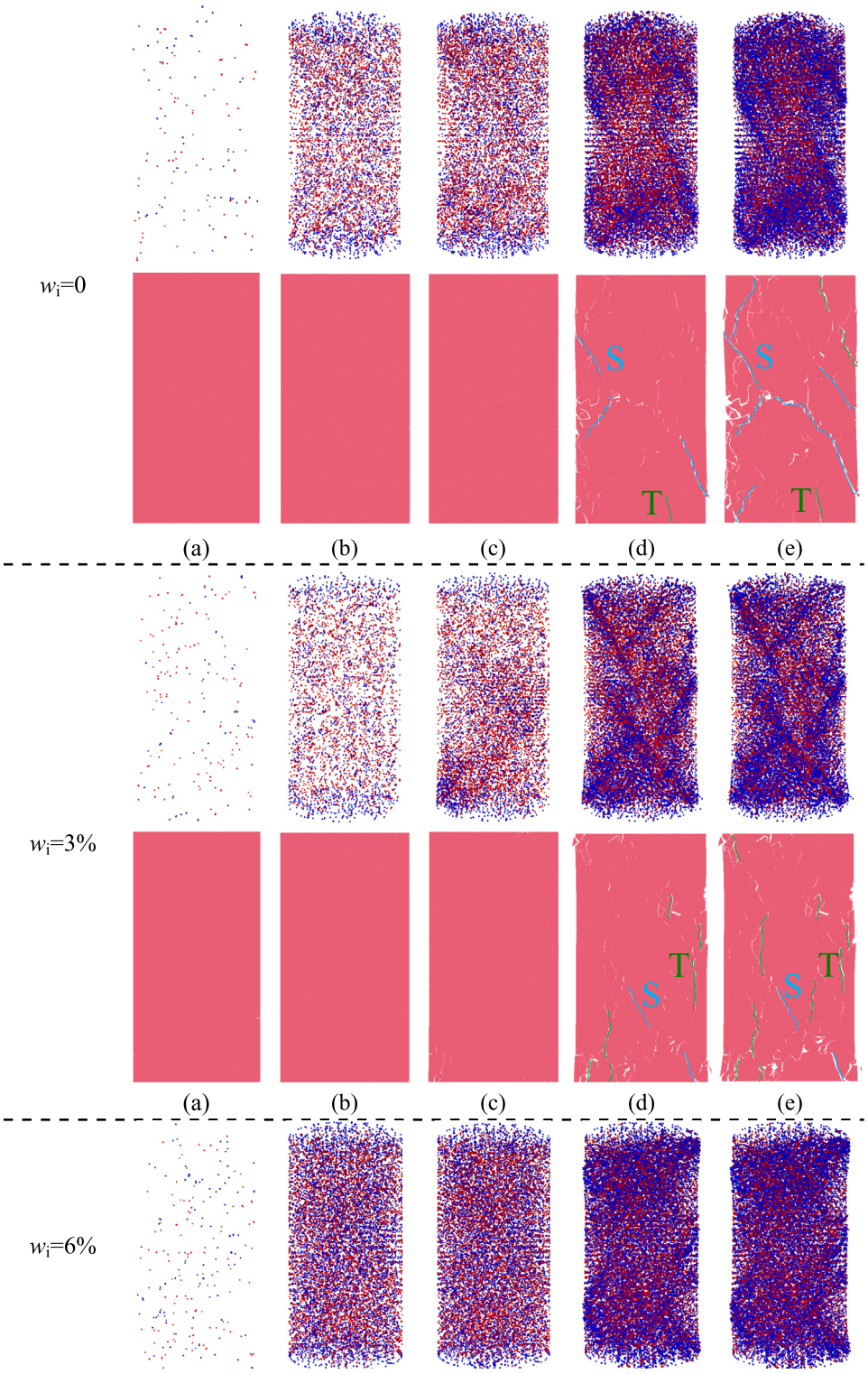

Fig. 20. 3D microcrack evolution process (red line-shear crack, blue line-tensile crack) and 2D macro failure modes of sulfate rock with different initial water content at (a) phase of crack initiation, (b) crack damage, (c) peak strength, (d) post-peak with 115% axial strain at peak strength, and (e) post-peak with 125% axial strain at peak strength under uniaxial compression test for modeling case.

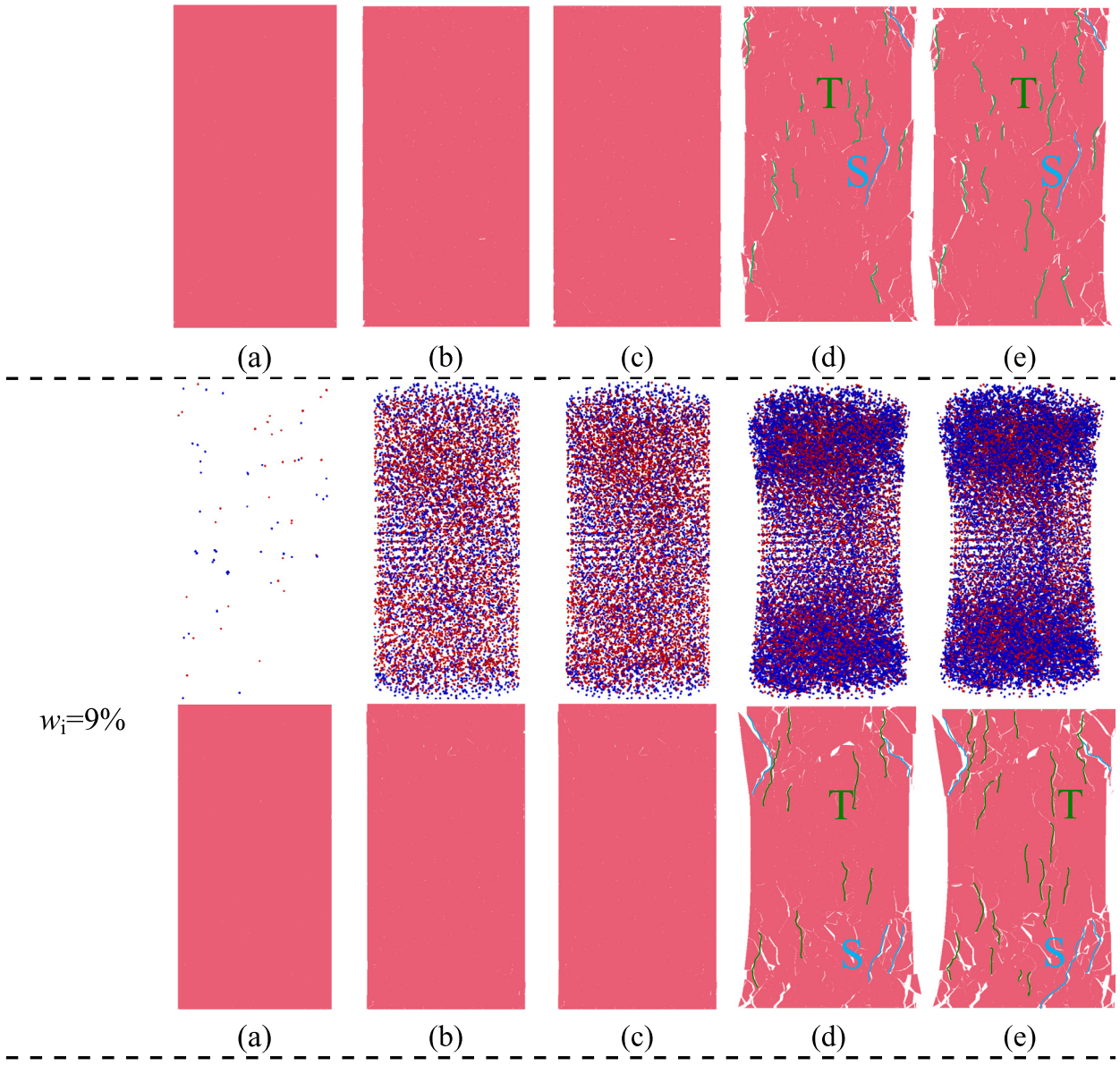

Fig 20. *(continued)*

Wanninger (2019) observed that sulfate rock forms distinct clusters of crystals following water absorption. Scanning electron microscopy (SEM) analysis revealed that these clusters consist of gypsum needle clusters. The formation of gypsum needle clusters leads to the development of microcracks within the specimen, which subsequently results in rock softening and strength degradation. The reduction in strength facilitates the initiation of tensile failure in both pre-existing microcracks and those induced by gypsum crystal growth, even under lower tensile stress, ultimately giving rise to macroscopic tensile cracks. The transformation of anhydrite into gypsum involves a dissolution process that creates voids, which are visible and thereby accelerate microcrack propagation. A higher initial water content leads to a greater extent of anhydrite-to-gypsum transformation, resulting in an increased number of microcracks. Macroscopically, this manifests as a gradual shift in the rock failure mode from shear-dominated to tensile-dominated behavior with increasing water content, accompanied by a marked reduction in uniaxial compressive strength (Wanninger, 2019).

5 Conclusions

In this study, a series of laboratory UCS tests and numerical three-dimensional DEM simulations were conducted on sulfate rock specimens to investigate the effects of initial water content on their macro- and meso-mechanical properties, as well as their failure behavior. The main conclusions of the study are as follows:

(1) This study successfully developed and validated the 3DEC-GBM modeling approach. Numerical simulations exhibited errors of less than 2.6% for Young's

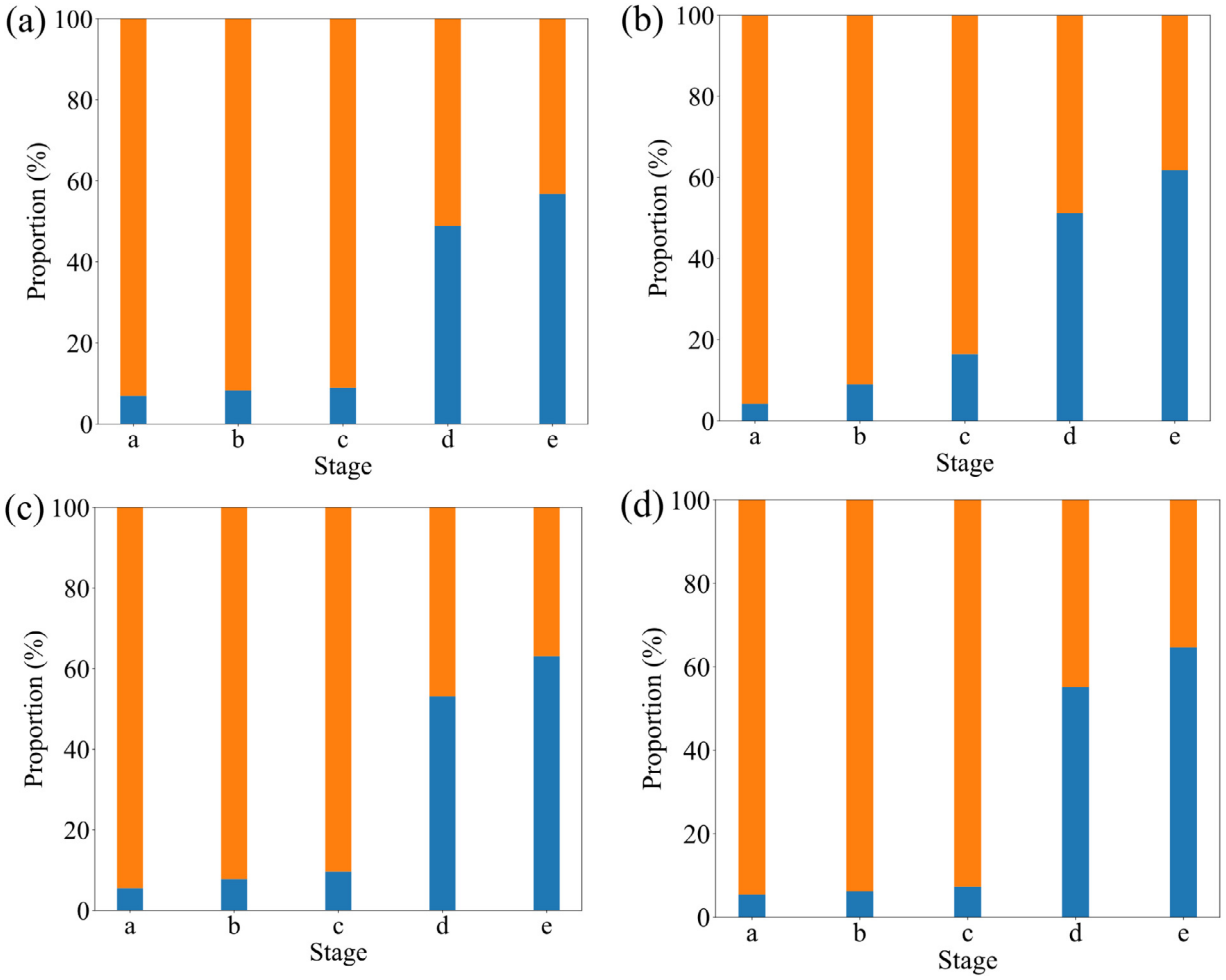

Fig. 21. Proportion of shear cracks and tension cracks in the total number of cracks at different stages in specimens with different initial water content of sulfate rock (blue represents tension cracks, orange represents shear cracks): (a) $w_i = 0$, (b) $w_i = 3\%$, (c) $w_i = 6\%$, and (d) $w_i = 9\%$.

modulus, Poisson's ratio, and peak stress, confirming the model's reliability in predicting the mechanical behavior of sulfate rock, particularly with respect to initial water content.

(2) Initial water content significantly affects the strength and deformation of sulfate rock. As water content increases from 0 to 9%, UCS decreases from 22.178 to 10.388 MPa, Young's modulus drops from 7.769 to 3.969 GPa, and Poisson's ratio rises from 0.10 to 0.39. Crack initiation stress (σ_{ci}) and crack damage stress (σ_{cd}) also decrease linearly with increasing water content.

(3) Higher water content accelerates rock damage and softening. The damage coefficient increases from 0.20 to 0.48, while the brittleness coefficient decreases from 4.08 to 1.08. Meso-mechanical parameters decline significantly: normal and shear stiffness drop by about 46.5%, peak cohesion reduces by 69.7%, and peak friction angle decreases by 17.39%. Meanwhile, peak tensile strength increases by 124%.

(4) Increased water content raises the proportion of micro-tensile fractures, shifting the dominant failure mode from shear to tensile failure. This highlights the critical role of water content in the stability and failure mechanisms of sulfate rock.

Data availability

The data that support the findings of this study are available from the corresponding author upon reasonable request.

CRediT authorship contribution statement

Li Yu: Writing – original draft, Formal analysis, Methodology, Investigation. **Youlin Qin:** Methodology, Investigation, Writing – review & editing, Formal analysis. **Hualao Wang:** Funding acquisition, Formal analysis, Writing – review & editing. **Mingnian Wang:** Supervision, Methodology, Writing – review & editing. **Zhaohui Chen:** Software, Investigation. **Mingyang Yu:** Writing – review & editing, Visualization, Data curation. **Hong Jin:** Writing – original draft, Investigation.

Declaration of competing interest

The authors declare that they have no known competing financial interests or personal relationships that could have appeared to influence the work reported in this paper.

Acknowledgement

This work was supported by the Special Science and Technology Innovation fund of Research Institute of Highway, Ministry of Transport of the People's Republic of China (Grant No. 2019-C505).

References

Alejano, L. R., Arzúa, J., Bozorgzadeh, N., & Harrison, J. P. (2017). Triaxial strength and deformability of intact and increasingly jointed granite samples. *International Journal of Rock Mechanics and Mining Sciences, 95*, 87–103.

Alonso, E., Berdugo, I., & Ramon, A. (2013). Extreme expansive phenomena in anhydritic-gypsiferous claystone: The case of Lilla tunnel. *Géotechnique, 63*(7), 584–612.

Alonso, E., & Ramon, A. (2013). Heave of a railway bridge induced by gypsum crystal growth: Field observations. *Géotechnique, 63*(10), 894.

Azocar, K. D. (2016). Investigating the mesh dependency and upscaling of 3D grain-based models for the simulation of brittle fracture processes in low-porosity crystalline rock. Queen's University (Canada), Doctoral dissertation.

Bornert, M., Vales, F., Gharbi, H., & Nguyen Minh, D. (2010). Multiscale full-field strain measurements for micromechanical investigations of the hydromechanical behaviour of clayey rocks. *Strain, 46*(1), 33–46.

Butscher, C., Breuer, S., & Blum, P. (2018). Swelling laws for clay-sulfate rocks revisited. *Bulletin of Engineering Geology and the Environment, 77*, 399–408.

Butscher, C., Einstein, H. H., & Huggenberger, P. (2011). Effects of tunneling on groundwater flow and swelling of clay-sulfate rocks. *Water Resources Research, 47*(11), W11520.

Butscher, C., Mutschler, T., & Blum, P. (2016). Swelling of clay-sulfate rocks: A review of processes and controls. *Rock Mechanics and Rock Engineering, 49*(4), 1533–1549.

Cherblanc, F., Berthonneau, J., Bromblet, P., & Huon, V. (2016). Influence of water content on the mechanical behaviour of limestone: Role of the clay minerals content. *Rock Mechanics and Rock Engineering, 49*(6), 2033–2042.

Farahmand, K., Vazaios, I., Diederichs, M. S., & Vlachopoulos, N. J. (2018). Investigating the scale-dependency of the geometrical and mechanical properties of a moderately jointed rock using a synthetic rock mass (SRM) approach. *Geotechnics, 95*, 162–179.

Gao, F., Stead, D., & Elmo, D. (2016). Numerical simulation of microstructure of brittle rock using a grain-breakable distinct element grain-based model. *Geotechnics, 78*, 203–217.

Gao, H., Liang, W. G., Yang, X., Zhang, C., Yue, G., & Zhang, P. (2011). Experimental study of mechanical property of gypsum rock soaked in hot saturated brine. *Chinese Journal of Rock Mechanics and Engineering, 30*, 935–943 (in Chinese).

Ghazvinian, E., Diederichs, M. S., & Quey, R. (2014). 3D random Voronoi grain-based models for simulation of brittle rock damage and fabric-guided micro-fracturing. *Journal of Rock Mechanics and Geotechnical Engineering, 6*(6), 506–521.

He, H., & Ahrens, T. J. (1994). Mechanical properties of shock-damaged rocks. *International Journal of Rock Mechanics and Mining Sciences, 31*(5), 525–533.

Huang, D., Tang, W., & Li, X. (2023). Numerical modeling and damage evolution research on the effect of joint geometrical parameters in nonpersistent jointed rock masses. *Bulletin of Engineering Geology and the Environment, 82*(4), 137.

Hu, D. W., Zhang, F., Shao, J. F., & Gatmiri, B. (2014). Influences of mineralogy and water content on the mechanical properties of argillite. *Rock Mechanics and Rock Engineering, 47*(1), 157–166.

Inga, C. E. C., Sinha, S., Walton, G., & Holley, E. (2023). Modeling Brazilian tensile strength tests on a brittle rock using deterministic, semi-deterministic, and Voronoi bonded block models. *Rock Mechanics and Rock Engineering, 56*(7), 5293–5313.

Itasca Consulting Group Inc. (2025). Three-dimensional Distinct Element Code (Version 9.1).

Kanit, T., Forest, S., Galliet, I., Mounoury, V., & Jeulin, D. (2003). Determination of the size of the representative volume element for random composites: Statistical and numerical approach. *Journal of the Mechanics and Physics of Solids, 40*, 3647–3679.

Kazerani, T., & Zhao, J. (2010). Micromechanical parameters in bonded particle method for modelling of brittle material failure. *International Journal for Numerical and Analytical Methods in Geomechanics, 34*(18), 1877–1895.

Lee, D. T., & Schachter, B. J. (1980). Two algorithms for constructing a delaunay triangulation. *International Journal of Computer & Information Sciences, 9*(3), 219–242.

Lemaitre, J. (2013). A course on damage mechanics. Springer Science and Business Media.

Li, Z. C., Zhu, Y., Zhou, H., & Li, J. (2022). Equivalent simulation method of humidity and temperature expansion for subway tunnels in swelling rock considering elastic softening. *Rock and Soil Mechanics, 43*, 497–507 (in Chinese).

Li, X. F., Li, H. B., Liu, L. W., Liu, Y. Q., Ju, M. H., & Zhao, J. (2020). Investigating the crack initiation and propagation mechanism in brittle rocks using grain-based finite-discrete element method. *International Journal of Rock Mechanics and Mining Sciences, 127*, 104219.

Li, X. F., Li, H. B., & Zhao, J. (2019). The role of transgranular capability in grain-based modelling of crystalline rocks. *Computers and Geotechnics, 110*, 161–183.

Liu, C. D., Cheng, Y., Jiao, Y. Y., Zhang, G.-H., Zhang, W. S., Ou, G. Z., & Tan, F. (2021). Experimental study on the effect of water on mechanical properties of swelling mudstone. *Engineering Geology, 295*, 106448.

Liu, Y., Yu, H., Wang, C., & Wang, C. (2011). Research on mechanism of damage of anhydrock in dolomite layer to tunnel structure. *Rock and Soil Mechanics, 32*, 2704–2708 (in Chinese).

Madsen, F., & Nüesch, R. (1991). The swelling behaviour of clay-sulfate rocks. *Proceedings of the ISRM Congress. ISRM.* .

Mardalizad, A., Scazzosi, R., Manes, A., & Giglio, M. (2018). Testing and numerical simulation of a medium strength rock material under unconfined compression loading. *Journal of Rock Mechanics and Geotechnical Engineering, 10*(2), 197–211.

Maximiliano, R. V., & Triantafyllidis, T. (2016). Influence of initial water content on the mechanical properties of an argillaceous swelling rock. *Rock Mechanics and Rock Engineering, 49*(7), 2555–2568.

Nicksiar, M., & Martin, C. J. (2012). Evaluation of methods for determining crack initiation in compression tests on low-porosity rocks. *Rock Mechanics and Rock Engineering, 45*(4), 607–617.

Pimentel, E., & Anagnostou, G. (2013). New apparatus and experimental setup for long-term swelling tests on sulphatic claystones. *Rock Mechanics and Rock Engineering, 46*(6), 1271–1285.

Pimentel, E. (2015). Existing methods for swelling tests–a critical review. *Environmental Earth Sciences, 76*, 96–105.

Schweizer, D., Prommer, H., Blum, P., Siade, A. J., & Butscher, C. (2018). Reactive transport modeling of swelling processes in clay-sulfate rocks. *Water Resources Research, 54*(9), 6543–6565.

Serafeimidis, K., & Anagnostou, G. (2014). On the crystallisation pressure of gypsum. *Environmental Earth Sciences, 72*, 4985–4994.

Serafeimidis, K., & Anagnostou, G. (2013). On the time-development of sulphate hydration in anhydritic swelling rocks. *Rock Mechanics and Rock Engineering, 46*(3), 619–634.

Serafeimidis, K., & Anagnostou, G. (2015). The solubilities and thermodynamic equilibrium of anhydrite and gypsum. *Rock Mechanics and Rock Engineering, 48*(1), 15–31.

Sinha, S., Shirole, D., & Walton, G. (2020). Investigation of the micromechanical damage process in a granitic rock using an inelastic bonded block model (BBM). *Journal of Geophysical Research: Solid Earth, 125*(3), e2019JB018844.

Sinha, S., & Walton, G. (2020). A study on bonded block model (BBM) complexity for simulation of laboratory-scale stress-strain behavior in granitic rocks. *Computers and Geotechnics, 118*, 103363.

Steiner, W. (1993). Swelling rock in tunnels: Rock characterization, effect of horizontal stresses and construction procedures. *International Journal of Rock Mechanics and Mining Sciences, 30*(4), 361–380.

Su, C., Wei, S., Xu, C., & Su, F. (2019). Experimental study on physico-mechanical effects of high temperature dehydrated gypsum rock. *Journal of Rock Mechanics and Engineering, 38*(2), 254–266 (in Chinese).

Turichshev, A., & Hadjigeorgiou, J. (2017). Development of synthetic rock mass bonded block models to simulate the behaviour of intact veined rock. *Geotechnical and Geological Engineering, 35*(1), 313–335.

Vásárhelyi, B. (2005). Statistical analysis of the influence of water content on the strength of the Miocene limestone. *Rock Mechanics and Rock Engineering, 38*(1), 69–76.

Vásárhelyi, B., & Ván, P. (2006). Influence of initial water content on the strength of rock. *Engineering Geology, 84*(1/2), 70–74.

Wang, X., & Cai, M. (2019). A comprehensive parametric study of grain-based models for rock failure process simulation. *International Journal of Rock Mechanics and Mining Sciences, 115*, 60–76.

Wang, X., & Cai, M. (2018). Modeling of brittle rock failure considering inter- and intra-grain contact failures. *Computers and Geotechnics, 101*, 224–244.

Wang, Y., Li, X., Ben, Y. X., Wu, Y. F., & Zhang, B. (2014). Prediction of initiation stress of dilation of brittle rocks. *Chinese Journal of Rock Mechanics and Engineering, 33*(4), 737–746 (in Chinese).

Wanninger, T. (2019). *Experimental investigations for the modelling of anhydritic swelling claystones*. ETH Zurich (Zurich), Doctoral dissertation.

Xu, C. B., Hao, X. Y., & Wei, S. J. (2019). Experimental study on uniaxial compressive strength of water immersed anhydrite. *Journal of Hydraulic Research and Development, 36*, 86–92 (in Chinese).

Xu, C. B., Zhou, X. Y., Wang, H. L., Gao, X. J., & Li, X. F. (2021). A case study of thaumasite sulfate attack in tunnel engineering. *Advances in Civil Engineering, 2021*, 1–14.

Yan, B., Kang, H., Li, X., Qi, Q., Zhang, B., & Liu, J. (2023). Damage constitutive model and mechanical properties of jointed rock mass under hydro-mechanical coupling. *Theoretical and Applied Fracture Mechanics, 123*, 103735.

Yang, J. P., & Du, F. Y. (2016). The influence of temperature and humidity effect on water absorption softening of swelling rock. *Science Technology and Engineering, 16*(20), 259–263 (in Chinese).

Yang, X., Yuan, X., Wu, Z., & Su, C. (2001). Experimental study on mechanical properties of blasting damaged rock. *Chinese Journal of Rock Mechanics and Engineering, 20*, 436–439 (in Chinese).

Zhang, C. L., & Rothfuchs, T. (2004). Experimental study of the hydro-mechanical behaviour of the Callovo-Oxfordian argillite. *Applied Clay Science, 26*(1/2/3/4), 325–336.

Zhang, H. J., Adoko, A. C., Meng, Z. J., Wang, H., & Jiao, Y. Y. (2017). Mechanism of the mudstone tunnel failures induced by expansive clay minerals. *Geotechnical and Geological Engineering, 35*(1), 263–275.

Zhang, K., Xia, K., & Liu, F. (2021). Simulation of rock failure by Voronoi-based discontinuous deformation analysis. *Chinese Journal of Rock Mechanics and Engineering, 40*, 725–738 (in Chinese).

Zhang, K. Y., Liu, F., Xia, K. W., Xu, Y., Dong, P., & Yu, C. Y. (2023). On the calibration and verification of Voronoi-based discontinuous deformation analysis for modeling rock fracture. *Journal of Rock Mechanics and Geotechnical Engineering, 15*(8), 2025–2038.

Zhang, Q. B., & Wu, K. (2020). Research on the strength and expansive characteristics of full weathered mudstone in Karawang area. *Journal of Railway Engineering Society, 37*(8), 15–19 (in Chinese).

Zhang, S., Jiang, Q., Qiu, S., Li, S., Kou, Y., & Xu, D. (2025). Assessment of strain bursting using a Voronoi-based breakable block model: A case study of 2400-m-deep tunnels. *Engineering Fracture Mechanics, 318*, 110930.

Zhang, S. K., Leng, X. L., & Sheng, Q. (2020). Study of water swelling and softening characteristics of expansive rock. *Rock and Soil Mechanics, 41*(2), 561–570 (in Chinese).

Zhao, X., Cai, M., Wang, J., Li, P., & Ma, L. (2015). Objective determination of crack initiation stress of brittle rocks under compression using AE measurement. *Rock Mechanics and Rock Engineering, 48*, 2473–2484.

Zhong, Z. B., Li, A. H., Deng, R. G., Wu, P. P., & Jun, X. (2019). Experimental study on the time-dependent swelling characteristics of red-bed mudstone in Central Sichuan. *Chinese Journal of Rock Mechanics and Engineering, 38*(1), 76–86 (in Chinese).

Zhu, Y. B., Wu, Y. L., & Yu, H. M. (2013). Strength behavior of tunnel's gypsiferous surrounding rock. *Journal of Yangtze River Scientific Research Institute, 30*, 53 (in Chinese).